Integrative single-cell analysis of neural stem/progenitor cells reveals epigenetically dysregulated interferon response in progressive multiple sclerosis

Bongsoo Park[1*], Alexandra M. Nicaise[2*], Dimitrios Tsitsipatis[3*], Liviu Pirvan[4], Pranathi Prasad[2], Miguel Larraz Lopez De Novales[4], Julia Whitten[1], Luka Culig[1], Joseph Llewellyn[1], Rosana-Bristena Ionescu[2], Cory M. Willis[2], Grzegorz Krzak[2], Jinshui Fan[3], Supriyo De[3], Marta Suarez Cubero[5], Angeliki Spathopoulou[5], Luca Peruzzotti-Jametti[2,6], Tommaso Leonardi[7], Frank Edenhofer[5], Myriam Gorospe[3], Irina Mohorianu[4°], Stefano Pluchino[2°], and Isabel Beerman[1°]

[1]Epigenetics and Stem Cell Unit, Translational Gerontology Branch, National Institute on Aging, NIH, Baltimore, MD, 21224 USA
[2]Department of Clinical Neurosciences and NIHR Biomedical Research Centre, University of Cambridge, Cambridge CB2 0AH, UK
[3]RNA Regulation Section, Laboratory of Genetics and Genomics, National Institute on Aging, NIH, Baltimore, MD, 21224 USA
[4]Wellcome-MRC Cambridge Stem Cell Institute, Jeffrey Cheah Biomedical Centre, University of Cambridge, Cambridge CB2 0AW, UK
[5]Department of Genomics, Stem Cell Biology and Regenerative Medicine & CMBI, Leopold-Franzens-University Innsbruck, Innsbruck, Austria
[6]Department of Metabolism, Digestion and Reproduction, Imperial College London, London SW7 2AZ, UK
[7]Center for Genomic Science of IIT@SEMM, Instituto Italiano di Tecnologia (IIT), 20139 Milan, Italy

[*]These authors contributed equally to this work.

Lead contact: Prof. Stefano Pluchino (SP), Email: spp24@cam.ac.uk

[°]**Corresponding author(s):** Dr Irina Mohorianu, email: iim22@cam.ac.uk; Prof. Stefano Pluchino (SP), Email: spp24@cam.ac.uk; Dr Isabel Beerman, email: isabel.beerman@nih.gov.

SUMMARY

Progressive multiple sclerosis (PMS) is characterized by a primary smoldering pathological disease process associated with a superimposed inflammatory activity. Cellular and molecular processes sustaining the pathobiology of PMS remain to be identified.

We previously discovered senescence signatures in neural stem/progenitor cells (NSCs) from people with PMS. Applying direct reprogramming to generate directly induced NSCs (iNSCs) from somatic fibroblasts, we retain epigenetic information and observe hypomethylation of genes associated with lipid metabolic processes and IFN signaling only in PMS lines. Single-cell/nucleus transcriptomic and epigenetic profiling reveal an inflammatory, senescent-like, IFN-responsive radial glia (RG)-like cell subcluster mainly in PMS iNSCs that is driven by IFN-associated transcription factors. Lastly, we identify a population of senescent, IFN-responsive, disease-associated RG-like cells (DARGs) in the PMS brain that share pseudotime trajectories with iNSCs *in vitro*.

We describe the existence of a non-neurogenic, dysfunctional DARG population that has the potential to fuel smoldering inflammation in PMS.

KEY WORDS

Neural stem/progenitor cells, radial glia, single cell/nuclei multiomics, direct reprogramming, RNA sequencing, DNA methylation, senescence, interferon, epigenetics, progressive multiple sclerosis.

INTRODUCTION

Multiple sclerosis (MS) is a complex neuroinflammatory and neurodegenerative disease characterized by inflammation and demyelination in the central nervous system (CNS). It is believed to be caused by an interplay of genetic predisposition and environmental risk factors, such as exposure to viruses.[1] The early phase of the disease, known as relapsing remitting MS (RRMS), pathologically manifests as acute demyelinating lesions with some endogenous repair. There are disease-modifying therapies (DMTs) available that target peripheral immune cells to reduce the risk of developing new lesions and clinical relapses. Over time, however, most people with RRMS transition into a progressive (PMS) stage of the disease that is characterized by the steady accumulation of neurological disability in the absence of endogenous repair that leads to neurodegeneration. Despite most available DMTs being effective in people with RRMS they are much less effective in people with PMS. This has made the progressive stage of the disease an unmet clinical need.[1]

Pathological, neuroimaging, and clinical data suggest that progressive MS is driven by a primary smoldering process associated with inflammation. Several mechanisms have been proposed to drive smoldering MS, including innate immune activation, demyelination and energy deficits, adaptive immunity, and, recently, age-related mechanisms.[2,3]

Age is one of the most significant risk factors in the development of PMS, which is similar to other neurodegenerative diseases such as Alzheimer's and Parkinson's disease.[4,5] Longitudinal assessment of brain aging using imaging technologies showed that people with MS demonstrate increased '*brain age*' compared to healthy controls that was defined by increased atrophy and decreased grey matter volumes.[6,7] Pathological hallmarks of cellular aging, such as senescence and senescence-associated changes, have been identified in people with PMS. These include decreased telomere length in peripheral leukocytes,[8-10] increased DNA and mitochondrial damage in neurons *in situ,*[11-13] increased epigenetic age in glial cells,[14] senescence-associated secretory phenotype (SASP) in microglia and astrocytes,[15,16] and p16/CDKN2A expression in glia and neural stem/progenitor cells (NSCs).[16,17] The increasing body of evidence suggesting an association of PMS with cellular senescence requires further study to understand how the accumulation of senescent glial cells contributes to disease pathogenesis.

The genetic components underlying MS risk and severity are incredibly complex. Genome wide association studies (GWAS) largely implicated cells of the peripheral immune system in the development of disease. However, mapping of MS susceptibility genes onto brain tissue has revealed enrichment of MS-susceptibility genes in glial cells of the CNS, including astrocytes, oligodendrocytes, and microglia. Moreover, prediction of MS severity from genetic

loci involved in the CNS were found to be associated with mitochondrial function, cellular senescence, and synaptic plasticity.[18]

Recent work with induced pluripotent stem cells (iPSCs), which retain the genetic information from the starting cell and is maintained in the resulting cell type of interest, has allowed for modeling of complex human brain disorders *in vitro*. Although iPSCs offer a powerful platform for modeling of human diseases, epigenetic modifications, especially those associated with aging, are lost in the reprogramming process due to the use of the Yamanaka factors.[19-21] Epigenetic changes, which can be reflected by environmental risk factors such as smoking and exposure to viruses, are likely contribute to MS susceptibility and progression. A few studies have identified aberrant DNA methylation patterns in both CNS tissue and peripheral blood and leukocytes in people with MS. Many of these patterns are associated with functional pathways related to immune response, neuronal survival[22], and demyelination.[23] Recent work has found that iPSC-NSCs from patients with PMS display markers of senescence and prevent oligodendrocyte progenitor cell differentiation via the SASP.[17,24] Furthermore, iPSC-astrocytes from MS patients also display senescence-related gene expression, dysfunctional metabolism, and increased immune and inflammatory genes.[25,26]

Stem cell exhaustion is a known hallmark of biological aging that is typically associated with reduced tissue repair. Adult brain stem cells/NSCs, also known as radial glia-like cells (RG), are astroglial-like cells that classically reside in the mammalian subventricular zone and dentate gyrus of the hippocampus and can give rise to mature neurons, astrocytes, and oligodendrocytes.[27] Furthermore, noncanonical niches for RG have also been reported, including the neocortex of primates,[28] the cerebellum of rabbits,[29] the amygdala of mice,[30] and the striatum of humans.[31] Studies in animals have shown that with progressing age and neurodegenerative disease the capabilities of RGs, such as differentiation into neurons and repair capabilities.[32-34] Many studies have attempted to address the existence, persistence, and role of NSC/RGs in the human brain following early post-natal life. Immunostaining of postmortem human brains[35] identified NSCs in the lining of the walls of the lateral ventricle, the dentate gyrus, and the olfactory epithelium.[36,37] However, their capacity for neurogenesis and differentiation, as well as their presence outside of the main CNS germinal stem cell niches is much debated.[38,39] More recently, phenomena such as inflammation and injury support both de-maturation of neurons[40] and de-differentiation of astrocytes[41] into NSC/RG-like cell states. NSCs expressing glial markers and displaying features of senescence have also been identified near lesioned areas in postmortem MS brain tissue.[17,42,43] Their role and putative function in brain physiology and disease is not currently understood.

Disease modeling with stem cell technologies holds the promise for understanding cellular dynamics that were previously unreachable in brain cells *in vivo*. We employed the use of direct reprogramming technology, which better retains epigenetic memory of the donor cells ,[44] to better investigate the origin of the senescent phenotype in NSCs within the context of PMS.[17,24,25,] We directly converted skin-derived fibroblasts from healthy human controls and people with PMS into stably expandable induced NSCs (iNSC). This was done by exposing fibroblasts to a transient (24-hour long) exposure to the Yamanaka factors[45] in the presence of NSC differentiation factors to generate a heterogenous population of stem and progenitor cells.

By subjecting both the parental fibroblasts and iNSCs to whole genome bisulfite sequencing (WGBS), we identified hypomethylated genes encoding proteins that function in pathways similar to those associated with inflammatory and interferon (IFN) signaling in PMS cells, suggesting a predisposition to inflammation. Furthermore, direct reprogramming to iNSCs maintained epigenetic information from the donor cells. Through both bulk and single-cell/ nucleus analysis, we found increased expression of gene pathways pertaining to cellular senescence, inflammation, and IFN signaling in a subset of PMS iNSCs. Combined single-nucleus ATAC seq supported changes in chromatin accessibility allowing for the enrichment of these pathways. Within the heterogenous iNSCs, we identify a unique inflammatory and senescent-like cluster and elevated expression of related upstream transcription factor IRF1 in PMS iNSCs. Lastly, we integrated published post-mortem single-cell/nucleus sequencing data sets and confirmed the presence of non-neurogenic, disease associated RG-like cells (DARGs) in the PMS brain, primarily in chronic active, slowly expanding lesions, exhibiting senescence and IFN-responsive characteristics.

Our work confirms that direct reprogramming technology is a powerful tool to model disease-in-a-dish to study neurodegenerative disorders. In doing so, it led us to identify the existence of a long-neglected, non-neurogenic DARG cell cluster especially in chronic brain MS lesions that has the potential to fuel continuous smoldering inflammation in PMS.

RESULTS

Bulk (multi-modal) sequencing reveals upregulation of senescence and inflammatory pathways in PMS iNSCs

To model disease and age associated NSC features, we directly reprogrammed skin-derived fibroblasts from control healthy subjects (Ctrl) and people with PMS (PMS) into stably expandable iNSCs (**Table S1**).[45] We confirmed the expression of established and accepted NSC markers, including the mRNAs, using RT-PCR, and proteins, using immunocytochemistry, that encode Nestin (NES), SOX2, ETNPPL, and PAX6, as well as the clearance of Sendai virus markers.[46] PCA population based mRNA sequencing (mRNAseq) (**Fig. 1A**) revealed robust signal across replicates and a clear separation between the Ctrl and PMS samples. Additional checks comprised incremental Jaccard similarity index (**Fig. S1A**),[47] and assessment and removal of technical noise using noisyR (**Fig. S1B**),[48] followed by normalization of expression levels.[47] The analysis of differences in the transcriptomes (with convergent results on the DESeq2[49] and edgeR[50] pipelines) led to 1,021 upregulated and 844 downregulated mRNAs (FDR < 0.05, $|\log2(FC)| \geq 0.5$) that included transcripts related to senescence, such as *CDKN1A*, *IRF7*, and *ISG15* (**Fig. 1B**). Gene set enrichment analysis (GSEA[51]), using all expressed mRNAs as background, identified several pathways enriched in the PMS iNSCs, including mRNAs encoded by gene sets that drive response to stress (*TNC*, *STAT6*), immune system processes (*THBS1*, *SPP1*), positive regulation of lipid metabolic process (*APOE*, *SREBF1*), regulation of cellular senescence (*CDKN1A*, *IGF1R*), interferon (IFN)-γ signaling (*ICAM1*, *HLA-DPB1*), and transcription factors associated with IFN signaling (*IRF-4*, *IRF-1*, *NF-kB*) (**Fig. 1C, Table S2**). Instead, mRNAs encoded by gene sets associated with cell cycle (*NASP, DPF1*) and telomere organization (*USP7, XRN1*) were all depleted in PMS iNSCs (**Fig. 1D**). This is concordant with previous work identifying cellular senescence in the NSCs of individuals with PMS.[17,24]

Next, we investigated the dynamics of gene regulatory networks (GRNs), using differentially expressed transcripts, associated with enriched terms (inflammation, regulation of cellular senescence, and interferon signaling). We observed a clear hub centered on the senescence gene *CDKN1A*, which then strongly interacted with *CDKN1C*, *CDKN2A*, *STAT1*, and *IRF1* in PMS iNSCs only (**Fig. 1E**). Previous studies have demonstrated that senescence induction via p21 (*CDKN1A*) and p16^{Ink4a} (*CDKN2A*) expression activates IFN response.[52] Density plots of covariation of inflammatory and senescent transcripts (selected based on GO annotations) showed greater difference in weights (i.e. interaction strength/ co-variation in expression) between Ctrl and PMS samples (with stronger covariation in the PMS samples), compared with non-differentially expressed transcripts (**Fig. S1C**). These results support the

203 predicted interactions between senescence and inflammation pathways.[52] This GRN analysis
204 also supports the hypothesis of an induction of a senescence program only in PMS iNSCs
205 that then promotes IFN and inflammatory signaling activities.

206 Because the sequencing data showed upregulation of genes associated with cellular
207 senescence, we independently validated these findings using Western blot and senescence-
208 associated β-galactosidase (SA-β-gal) staining. We found upregulation of markers of cellular
209 senescence p16^{Ink4a} and GDF15 (**Fig. 1F**)[53] and increased expression of SA-β-gal using
210 SPiDER-β-gal dye in all PMS lines (**Fig. 1G**).[54] Cellular senescence is primarily associated
211 with a halt in cell cycle, which was supported by a depletion of cell-cycle pathways in the
212 mRNAseq (**Fig. 1D**). We then assessed the cycling stage of iNSCs using flow cytometry.
213 Despite iNSCs being analyzed under proliferative conditions in chemically-defined media, we
214 still identified a significantly higher proportion of PMS iNSCs in the G1 phase of the cell cycle
215 (*vs* Ctrl), which is typical of quiescent or senescent cells (**Fig. 1H**).[55] Lastly, quantitative
216 (q)PCR-based analysis of relative telomere length revealed that PMS iNSCs have significantly
217 decreased telomere lengths (*vs* Ctrl) (**Fig. 1I**).

218 Therefore, PMS iNSCs phenotypically display intrinsic features of senescence, which are
219 also reflected at the transcriptomic level via upregulation of pathways associated with
220 inflammation and IFN signaling.

221

222

223 **PMS fibroblasts and iNSCs maintain pathological epigenetic hallmarks**

224 We further investigated the potential origin of the senescent and inflammatory
225 transcriptomes and phenotypes seen in PMS iNSCs. We postulated that the direct conversion
226 from fibroblasts into iNSCs would maintain or even facilitate the emergence of new epigenetic
227 landscapes that further promote the senescence phenotype.

228 To this aim, we assessed the methylation status, genome-wide, using whole genome
229 bisulfite sequencing (WGBS) on the parental fibroblasts and matched iNSC lines. PCA
230 revealed a tight reproducibility of replicates and a clear separation between fibroblasts and
231 iNSCs as well as between Ctrl and PMS samples (**Fig. 2A**).

232 We identified 28 million CpG sites per sample and consistently observed increased
233 hypermethylation in iNSCs (*vs* fibroblasts) (**Fig. S1D-E**). To provide insight to the extent the
234 direct reprogramming reset the aging-related epigenome, we assessed the Cortex Age DNA
235 methylation (DNAm) aging clock using methylation data from the human cortex.[56] The cortex
236 clock predicted an age similar to the chronological age of the donor cells used to generate the
237 iNSCs, suggesting minimal epigenetic resetting occurred during the direct reprogramming

238 (**Fig. 2B**). We also matched this modality against the Horvath and Zhang DNAm clocks, which
239 further confirmed the maintenance of epigenetic age after direct reprogramming for most cell
240 lines (**Fig. S1F**).[57,58] Thus, our own direct reprogramming technology to generate iNSCs from
241 skin-derived fibroblasts maintains epigenetic information from the donor cells.

242 We next investigated methylation commonalities and specific differences between Ctrl and
243 PMS samples in both fibroblasts and iNSCs. We assessed the distribution of differentially
244 methylated regions (DMRs) across genic and intergenic annotations, including a class linking
245 the DMR to the transcription start sites (TSS) and the resulting distribution was quasi uniform
246 (**Fig. S1G-H**). The differentially methylated cytosines (DMCs) and DMRs indicated an
247 increased hypomethylation in both PMS fibroblasts and iNSCs (*vs* Ctrl; **Fig. 2C, Fig. S1I**). To
248 further explore how these differences in methylation profiles account for transcriptional and
249 phenotypic changes, we investigated genes with hypomethylated DMRs located in proximity
250 of the TSSs. We identified 4,743 genes hypomethylated only in PMS fibroblasts, 3,133 genes
251 hypomethylated only in PMS iNSCs, with 2,344 hypomethylated genes shared between PMS
252 fibroblasts and iNSCs (**Fig. 2D**).

253 We performed GSEA on the specific hypomethylated genes of the PMS fibroblasts, and
254 found pathways associated with T cell activation, IL-12 production, and JAK-STAT signaling
255 (**Fig. 2E, Table S3**). This was further supported enriched motifs associated with transcription
256 factors in the PMS fibroblasts. These include *SREBP1*, known to regulate T cell growth and
257 survival, as well as *DDIT3*, which is closely connected to JAK-STAT signaling (**Fig. S1J**).[59,60]
258 Gene pathways specific to hypomethylation PMS iNSCs included cytokine production, TNF
259 superfamily cytokine production, and regulation of I-κB kinase/NF-κB signaling (**Fig. 2F**).
260 Additional analyses of enriched motifs identified *STAT5* and *IRF6*, encoding proteins known
261 to be involved in cytokine production, immune response, and senescence (**Fig. S1J**),[61,62] and
262 *ARID5A*, which encodes a protein involved in the immune response by stabilizing *IL-6* mRNA
263 (**Fig. 2F, Fig. S1J**).[63]

264 To determine which gene pathways were retained in the epigenome between the PMS
265 fibroblasts and iNSCs, we performed GSEA on genes commonly hypomethylated in both cell
266 types. The results revealed genes encoding proteins with functions in pathways associated
267 with lipid metabolism, inflammation, and IFN production (**Fig. 2G**). In a separate study, we
268 performed metabolomics and lipidomics on the same Ctrl and PMS cell lines, which led to the
269 identification of increased cholesterol synthesis in PMS iNSCs and a new role for this pathway
270 in establishing and sustaining their pathological and neurotoxic phenotype.[46] In addition, using
271 published GWAS data genes associated with MS progression and pathology were identified
272 such as leukocyte activation and differentiation, STAT signaling, and IFN production.[64-66]

273 Another example is *IRF5*, known to have associated gene variants in MS,[67] which we found
274 hypomethylated at the promoter-TSS region, in both PMS fibroblasts and iNSCs (**Fig. 2H**).

275 We also analyzed hypermethylated genes, with DMRs located in the promoter regions and
276 in proximity of the TSS. We found 2,946 genes specifically hypermethylated in PMS fibroblasts
277 (*vs* Ctrl), 858 specifically hypermethylated in PMS iNSCs (*vs* Ctrl), and 291 shared
278 hypermethylated genes (PMS fibroblasts *vs* Ctr iNSCs) (**Fig. S1K**). Analysis of the unique
279 differentially hypermethylated genes revealed differences in pathways associated with RNA
280 metabolic processes and cell cycle in fibroblasts and pathways associated with transcription
281 and neuronal differentiation in iNSCs (**Fig. S1L-M**). The hypermethylation pattern of genes
282 that is shared between PMS fibroblasts and iNSCs included DNA-templated transcription and
283 telomerase holoenzyme complex assembly (**Fig. S1N**).

284 To further investigate the epigenetic regulatory modules defined from the WGBS dataset,
285 we used denovo and directed HOMER analysis is to assay for enrichment of shared binding
286 motifs between the PMS fibroblasts and iNSCs, which identified NF-κB, a major transcription
287 factor that regulates genes responsible for both the innate and adaptive immune response
288 and is associated with senescence (**Fig. 2I**).[66,68,69] These results were corroborated by the
289 GSEA of the mRNAseq data, where an enrichment in genes associated with NF-κB was also
290 observed in the PMS iNSCs (**Fig. 1C**).

291 Our data suggest that PMS pathology is strongly linked to alterations of the epigenome,
292 which we identified first in patient fibroblasts and confirmed in iNSCs. Many of these epigenetic
293 differences are features of senescence and involve genes that regulate inflammatory,
294 metabolic/lipid, and IFN pathways. Furthermore, when PMS fibroblasts are directly
295 reprogrammed into iNSCs they also adopt an epigenetic landscape that is permissive for
296 increased expression of proteins associated with secretion of inflammatory cytokines,
297 specifically IL-6 and TNF- α.

298

299

300 **iNSCs share an RG-like signature that is identified in transcriptomic signatures from**
301 **postmortem human datasets**

302 Next, we explored the heterogeneity of iNSCs and the respective subpopulations driving the
303 phenotypes observed in mRNAseq and WGBSseq sequencing.

304 We first performed single cell (sc) and single-nucleus (sn) RNAseq coupled with ATAC
305 sequencing on the Ctrl and PMS iNSCs to determine if there was a subpopulation of cells that
306 were driving the phenotypes observed in the mRNAseq and WGBSseq (**Fig. S2A**). To
307 minimize technical discrepancies between the two approaches, data-driven, specific filters

308 were applied, on the proportions of reads incident to mitochondrial (MT) DNA and ribosomal
309 proteins (RP). We retained cells with 15-40% RP ratios for the scRNAseq samples and 2-25%
310 RP ratios for the snRNAseq data samples; across the dataset, a 20% MT ratio filter was
311 applied (**Fig. S2B-C**). Additional filters rely on number of UMIs > 8,000, number of genes per
312 cell > 1,000, $\log_{10}$ (genes per UMI) > 0.75. A total of 26,138 cells, across all samples, passed
313 all filtering criteria, with median UMI counts per cell of 22,296. The average number of cells
314 per sample was 3,267, ranging from 1,277 to 5,545; the average number of genes per cell
315 was 5,725, ranging from 4,357 to 6,731 (**Fig. S2D-E**).

316 Using these filtering criteria for RNA analysis, we identified a total of 8 clusters (**Fig. 3A**).
317 We applied the ClustAssess[70] framework to determine the optimal parameters in a data-driven
318 way using the Element Centric Similarity (ECS)[71] as assessment criteria for the crisp
319 partitioning of cells. The type of features (highly variable or most abundant) and number of
320 features retaining signal (i.e. not biased by noise or shallow sequencing) were first determined
321 on 20 iterations of ECS and summarized as element centric consistency (ECC). Next the
322 number of neighbors for the community detection approach and the clustering method was
323 also determined on high ECC distribution. The stable configurations linked number of clusters,
324 number of the most frequent partition, and the resolution parameter (**Fig. S2F-G**). The
325 distribution of ECC across the UMAP indicated a high stability for the selected number of
326 clusters (**Fig. 3B**). We observed a quasi-uniform distribution of cells across all samples and
327 conditions for all clusters (**Fig. S2H**).

328 An indirect assignment of cluster identity was based on expression of standard transcripts
329 for radial glia (RG), astroglial progenitors, and neuronal progenitors (gene lists in **Table S4**).
330 We found that a majority of the iNSC clusters were defined by an RG-gene or astroglial
331 progenitor gene signature, including the expression of *SOX2*, *NES*, *PAX6*, *PTPRZ1*, *HES1*,
332 and *CKB* mRNAs (**Figs. 3C-D**). The majority of clusters (0-3, 5-7) had a radial glia and/or
333 astroglial progenitor gene signature, encompassing 20-80% of cells within each individual
334 cluster, using defined mRNA thresholds (**Fig. S2I-J**). We also found a small proportion of
335 neural progenitor cells primarily represented by cluster 4 (**Fig. 3E, Fig. S2K**). Transcripts
336 associated with cell differentiation, including oligodendrocyte progenitor cells (*PDGRA*),
337 oligodendrocytes (*OLIG1*, *OLIG2*, *MBP*), astrocytes (*AQP4*, *ALDH1L1*), and mature neurons
338 (*CALB*, *CCK*) were lowly expressed across the samples and clusters (**Fig. S2L,** gene list in
339 **Table S4**).[72-75] This initial voting-scheme analysis suggests that proliferating iNSCs – similarly
340 to hiPSC-NSCs[76] – are a heterogenous population of cells displaying a transcriptional
341 signature reminiscent of RG-like, astroglial progenitor cells, and a small subpopulation of
342 neural progenitor cells, with little to no detection of terminally differentiated cells.

343 We next assessed the proportion of cells belonging to either Ctrl or PMS iNSCs within the
344 individual clusters. Strikingly, we found mostly equal representation amongst all clusters but
345 cluster 5, which was significantly enriched with PMS iNSCs (**Fig. 3F**). Towards further
346 understanding the biological role of the individual clusters we performed GSEA. Core clusters
347 0, 1, and 3 were enriched for terms linked to CNS development, gliogenesis, and proliferation,
348 while depleted of terms associated with cellular differentiation and pluripotency (**Fig. 3G, Table**
349 **S5**). Cluster 4 was enriched in pathways related to neuronal and cortical development, with a
350 coordinated depletion in the mitotic cell cycle genes (**Fig. 3H**). The remaining clusters were
351 associated with mitochondrial organization and oxidative phosphorylation (cluster 2), glial cell
352 differentiation (cluster 6), and ion transport (cluster 7) (**Fig. S3A-C**). Cluster 5, showing a
353 striking 6-fold higher frequency in PMS iNSCs (85.6% PMS *vs* 14.4% Ctrl) (**Fig. 3F**), was
354 characterized by genes enriched for cytokine production, immune processes, and IFN
355 signaling, and genes depleted for proliferation and regeneration (**Fig. 3I**).

356 To evaluate the contribution of cell cycle genes to the transcriptomics signature of clusters,
357 we identified the cell cycle stage using *a priori* cell cycle genes. We note a strong
358 representation of cells expressing G1-phase specific mRNAs in cluster 4, a depletion of cells
359 expressing G1-phase specific mRNAs in clusters 1, 2, 3, and a depletion of cells expressing
360 S-phase specific mRNAs in cluster 5, which further supports the GSEA analysis per cluster
361 (**Fig. S3D**).

362 To investigate the relevance of the *in vitro* iNSC model to human disease, we aligned our
363 *in vitro* results with two independent, publicly available *ex vivo* human snRNAseq datasets
364 from post mortem MS cases and controls.[16,77] Using a panel of canonical RG transcripts that
365 were also used to characterize the iNSCs (**Table S4**), we identified disease associated RG-
366 like cells within the annotated astrocyte clusters in both datasets (ranging between 6.5 – 7.8%
367 of total astrocyte cluster, **Fig. 3J-K**). When compared to the non-RG-like cells within the
368 astrocyte cluster, RG-like cells exhibited a significantly higher proportion and expression of
369 RG transcripts *ETNPPL*, *PTPRZ1*, *SOX2*, *PAX6*, and *PCNA* encoding a cell cycle marker (**Fig.**
370 **S3E-F**). RG-like cells expressed astroglial mRNAs (**Fig. 3C-D**) and very little microglia-specific
371 or oligodendrocyte progenitor cell-specific mRNAs (**Fig. S3E-F**), further supporting their
372 identity. To determine whether these newly identified RG-like cells hold neurogenic potential,
373 we assessed related transcripts, including *SOX11*, *DCX*, and *TUBB3* and found little
374 expression in both RG-like and non-RG-like cells within the astrocyte cluster in both datasets
375 (**Fig. S3G**). A large proportion of the RG-like cells expressed mRNAs specific of G2M or S
376 phases, which indicated their ability to progress through the cell cycle (**Fig. S3H**). Lastly, we
377 assessed the proportion of RG-like cells across the different MS lesion types. Out of all the

378 RG-like cells in both datasets, we identified that 50% were in chronic active lesions, whereas
379 the smallest proportion of cells were found in control tissue (**Fig. 3L-M**).

380 Therefore, we identify a small proportion of non-neurogenic RG-like cells in the healthy
381 adult human brain, which significantly increase in frequency in chronic active lesions in the
382 PMS brain.

383

384

385 **Patient iNSCs harbor a senescent, IFN-responsive RG-like cell cluster reminiscent of**
386 **Disease Associated RG the PMS brain**

387 As cluster 5 was predominant in PMS iNSCs (*vs* Ctrl), we sought to further the disease-
388 associated transcriptomic signature of this cluster. Transcriptionally across all samples, cluster
389 5 showed a significant enrichment of mRNAs associated with cellular senescence, IFN α/β
390 signaling, and RIG-I signaling, along with a depletion of mRNAs associated with cell
391 proliferation, DNA-templated transcription, and NOTCH1 signaling (**Fig. 4A**). Cluster 5 also
392 had the highest expression of mRNAs associated with IFN-α and -γ response and the
393 SenMayo gene set[78] (*vs* core clusters 0-3) (**Fig. 4B**). We performed a differential expression
394 analysis followed by GSEA of cluster 5 only and identified a strong enrichment for IFN and
395 cytokine signaling pathways and SASP that was associated with high expression of *IFIT1*,
396 *ISG15*, and *NLRP2* in PMS iNSCs (*vs* Ctrl) (**Fig. 4C**). We confirmed the high expression of
397 IFN-response transcripts (*IFIT1*, *IFIT2*) was linked to the hypomethylated promoter regions
398 associated with IFN signaling seen in both PMS fibroblasts and iNSCs, identified in WGBS
399 analysis (**Fig. 2H**).

400 We next wanted to assess the expression of SenMayo and IFN α/β signaling gene sets in
401 RG-like cells from the two human *ex vivo* snRNAseq datasets[16,77] of postmortem MS brains
402 (**Fig. 4D-E**). A proportion (16-28%) of total RG-like cells – which we termed Disease
403 Associated RG (DARGs) – in chronic lesions showed non-zero expression of the SenMayo
404 gene set, whereas <5% of RG-like cells with the same features were identified in control
405 tissues (**Fig. 4F-G**, **Fig. S4A-B**). We also identified an enrichment in IFN-associated mRNAs
406 in DARGs located in chronic active lesions (**Fig. 4H-I, Fig. S4C-D**).

407 We wanted to determine whether the senescence and IFN-associated gene expression
408 profiles are unique to DARGs by applying the same thresholds to the non-RG-like cells and
409 analyzing the datasets. Within chronic active lesions we identified a ~2.3-fold increase in the
410 proportion of senescent DARGs (*vs* senescent non-RG-like cells) in both datasets[16,77] (**Fig.**
411 **S4A-B**). We then compared all lesion areas and identified a ~2-fold increase in the fraction of
412 senescent DARGs in the edge of chronic active lesions, when compared to lesion core,

chronic inactive lesion edge, periplaque white matter, and control white matter[16,77] (**Fig. S4A-B**). DARGs in *Absinta et al.*[16] showed high expression of IFN-associated mRNAs (*vs* non-RG-like cells) in chronic active lesions (**Fig. S4C**), while displaying the same trend in chronic inactive lesions in *Schirmer et al.*[77] (**Fig. S4D**).

These findings provide further support to the existence of non-neurogenic DARGs in the PMS brain, particularly in chronic active lesions, with an inflammatory and senescent transcription signature. Notably, the direct reprogramming of patient somatic cells into stably expandable iNSCs allows for the recapitulation of distinctive disease-associated cellular phenotypes and gene signatures found in the postmortem MS brain.

Disease associated senescent RG-like cells spread dysfunctional features towards other clusters

We then performed pseudotime analysis to better understand the developmental trajectories of the RG-like cell cluster of PMS iNSCs with senescent and inflammatory signatures (**Fig. 5**). We removed the neural progenitor-associated cells (cluster 4) which allowed our analysis to focus on the establishment of inflammatory cluster 5. The initialization of the pseudotime focused on cluster 5, defined as the endpoint. The predicted trajectory started with core clusters 0, 1, and 3, progressed to cluster 2 and ending in cluster 5 (**Fig. 5A**). A community-based clustering was applied on the gene expression levels, with the stability assessed using ClustAssess.[70] Several gene modules i.e. clusters of genes with similar expression profiles across the pseudotime were predicted (**Fig. S4E**). We focused on three gene modules with distinct expression patterns. The expression profile of the first module (module 10) focused on the core clusters 0, 1, and 3. A gene enrichment analysis identified significantly elevated expression of mRNAs associated with cell cycle terms, as well as TFs known to maintain NSC/RG identity such as *SP2* (**Fig. 5B, Table S6**).[79] Module 3, which consisted of mostly cells assigned to cluster 2, showed enrichment in terms associated with mitochondria and antigen processing and presentation, including NSC/RG-associated TFs *E2F1* and *PAX6* (**Fig. 5C**). These results support the GSEA enrichment on cluster 2 characterized by mitochondrial and metabolic gene pathways (**Fig. S3B**). Module 7 mostly overlapped with cells in cluster 5 and exhibited enrichment in IFN and cytokine signaling pathways, as well as TFs associated with IFN signaling (*IRF3*, *STAT2*) (**Fig. 5D**). This suggests that the progression towards cluster 5 may originate in iNSCs with a cluster 2-like gene signature and display pathways associated with mitochondria and cellular metabolism. Therefore, an altered metabolic signature in PMS iNSCs, which we have recently described,[46] may promote the resurgence of the newly identified IFN responsive RG-like cell cluster 5.

449 Using the modules derived from the *in vitro* dataset, we next identified cells with similar
450 transcriptomic signatures in the *ex vivo* postmortem datasets.[16,77] Focusing on the
451 recalculated *ex vivo* UMAPs and underlining the RG-like cells (**Fig. 3J-K**), we inferred
452 pseudotime trajectories on both datasets using the core of the RG-like cells (clusters 0, 1, 3)
453 as an initialization point. (**Fig. 5E-F**). Next, we matched the gene modules determined in the
454 *in vitro* and *ex vivo* datasets, respectively. Using the gene lists from the individual modules we
455 cross-referenced the gene modules from the *in vitro* perspective (**Fig. 5B-D**, **Table S6**) and
456 from the *ex vivo* perspective (**Fig. S4F-G**). For the *Absinta et al.* dataset we found coordinated
457 gene expression within modules 5 and 7 that matched our *in vitro* curated modules and module
458 7 matched the inflammatory, senescent cluster 5 (**Fig. 5E, G**) and was associated with DARGs
459 in the chronic active lesion (**Fig. 5G**). In the *Schirmer et al.* dataset we found coordinated gene
460 expression within modules 4 and 7 (**Fig. 5F, H**). Genes that strongly contributed to module 7
461 were associated with chronic inactive lesions (**Fig. 5H**).

462 This analysis highlights the identification of a new cluster of senescent-like, inflammatory
463 non-neurogenic DARGs stemming from astrocyte-like cells in the postmortem MS brain.

464 As senescence is associated with and perpetuated by secreted proteins, we next
465 investigated ligand-receptor interactions between cluster 5 (as source of ligands) and other
466 clusters (as source of receptors) in iNSCs using NicheNet[80]. With this modeling, Ctrl iNSCs,
467 were enriched for ligand-receptor interactions regulating cell maintenance and differentiation
468 (i.e., Notch signaling) (**Fig. 5I**).[81] However in PMS iNSC, modelling predicted strong
469 interactions between TRAF2 in cluster 5 with TNFRSF1B in clusters 0, 1, and 3, which
470 anticipates induction of NFκB activation[82] and NSC activation,[83] along with a depletion in Wnt
471 signaling via LRP6 (**Fig. 5J-K**).

472 Next, we performed a cluster-by-cluster GSEA analysis and found that clusters 0, 1, and 3
473 in PMS iNSCS were enriched for senescence pathways, particularly those associated with
474 DNA damage and corresponding depleted for proliferation-related terms (**Fig. 5L, Table S7**).
475 We also detected significant interactions between *COL2A1* from cluster 5 and integrin-based
476 receptors in cluster 2 (*ITGB8*, *ITGAV*, *GP6*), coupled with a depletion in NOTCH1 signaling
477 (**Fig. 5J-K**). Enrichment analysis of genes in cluster 2 of PMS iNSCs further indicated
478 enrichment in senescence, IFN signaling, and ECM and corresponding depletion in
479 differentiation and DNA transcription that is known to be regulated by NOTCH signaling (**Fig.
480 5L**). Analysis of clusters 4, 6, and 7 consistently identified enrichment of inflammatory-
481 associated terms (i.e., neurodegeneration, oxidative stress-induced senescence, and
482 signaling by Ils) and a depletion in terms associated with NSC maintenance (i.e., Wnt signaling
483 and cell cycle) (**Fig. S4H**). The enrichment in inflammatory terms in PMS iNSCs were linked

484 to increased inflammatory interactions, stemming from cluster 5, between CCR3-CCL5 and
485 between A2M-MMP2 (**Fig. 5J**).

486 To further test the hypothesis that the ligand-receptor interactions predicted above are
487 relevant, we ran a cytokine array on the conditioned media (CM) from the bulk iNSC lines.
488 Quantification of the cytokine array confirmed an increased secretion of cytokines associated
489 with the SASP[84] and inflammation (IL-6, IGFBP-3, and TNFα) in PMS iNSCs (*vs* Ctrl) (**Fig.**
490 **5M**).

491 We then quantified the expression levels of the genes coding for the upregulated SASP
492 (**Fig. 5M**) using our mRNAseq data (**Fig. 1A-E**). Both *TIMP2* and *IGFBP2*, along with the
493 known SASP gene *GDF15*, were upregulated both at gene and protein levels (**Fig. 1F** and
494 **Fig. 5M-N**). Next, we re-analyzed the single-cell data for the genes and proteins associated
495 with the secreted factors identified in the mRNAseq and cytokine array, respectively, and
496 confirmed the elevated expression in cluster 5 of *TNF*, *FN1*, and *ISG15* (**Fig. 5O**).

497 Overall, our findings suggest that the developmental trajectories of RG-like cells in cluster
498 5 arise from cluster 2. Additionally, PMS iNSCs secrete inflammatory factors as part of their
499 SASP, and that this may induce a dysfunctional, senescent phenotype in cells in other clusters.

500

501

502 Integrative multi-omics reveals regulons defining inflammatory RG-like cell in 503 PMS iNSCs

504 To further investigate the epigenetic mechanisms that may contribute to the unique
505 transcriptome of the PMS iNSC cluster 5, we integrated the RNAseq data with single-nuclei
506 chromatin accessibility data (snATACseq) using both matched and un-matched samples. For
507 a high proportion of cells, we matched RNA and ATAC expression distributed proportionally
508 across clusters (**Fig. S5A**). Next, we selected data-driven parameters and stable configuration
509 (high ECC scores) on the ATAC modality using 30 iterations (**Fig S5B-D).** ClustAssess
510 identified 8 clusters from the ATACseq dataset.

511 We then matched the RNA clusters onto the ATAC UMAP, and the ATAC clusters onto the
512 RNA UMAP, respectively to evaluate the concordance of the two modalities (**Fig. 6A-B**). Next,
513 we quantified the equivalence between the RNA and ATAC clusters by summarizing matching
514 cell types/states, which allowed highlighting a match between RNA cluster 5 and ATAC cluster
515 8, well separated in the non-linear space from the other cells (**Fig. 6C**). Then, we confirmed
516 that the inflammatory ATAC cluster 8 was primarily composed of PMS iNSCs (**Fig. S5E**).

517 We also examined differentially accessible regions (DARs) specific to inflammatory ATAC
518 cluster 8, by selecting the corresponding peaks and identifying enriched motifs associated
519 with TFs. Our analysis identified DARs that gained accessibility were associated with immune
520 processes, IFN signaling, and cytokine production (*IRF3*, *STAT2*), and DARs that lost
521 accessibility were associated with genes pertaining to neuron and astrocyte differentiation and
522 neural crest cell fate specification (*SOX4*, *SOX8*) (**Fig. S5F, Table S8**).

523 We next assessed the overlapping motifs significantly enriched for epigenetic changes in
524 both PMS fibroblasts and iNSCs from the WGBS and from the predicted signature genes of
525 RNA cluster 5 and identified common TFs including *p53*, *E2A*, and *SMAD2* (**Fig. S5G**). As *p53*
526 and *E2A* are implicated in promoting immune function, involved in senescence, and in
527 mediating IFN responses,[85,86] our findings suggest that the chromatin accessibility for RNA
528 cluster 5 closely predicts its RNA expression signature. Biologically, these cells are strongly
529 IFN-responsive and display RG-like signatures. Our identification of common motifs
530 maintained from the fibroblasts during reprogramming to iNSCs in PMS cell types further
531 confirms the involvement of epigenetic regulation in perpetuating the senescent and IFN-
532 response in the iNSCs.

533 Since IFN signaling was found to be strongly involved in RNA cluster 5, we next investigated
534 the chromatin accessibility at the promotor regions. We identified increased accessibility at
535 *IFIT1* in ATAC cluster 8, corresponding to increased expression of this transcript in RNA cluster
536 5 (**Fig. S5H**). We next investigated genes that are known targets of the known regulator of
537 *IFIT1*, *IRF1*, which we identified to be enriched in the mRNAseq of the bulk PMS iNSCs (**Fig.**
538 **1C**). *IRF1* is a key transcription factor implicated in facilitating TNF-α-induced senescence and
539 is known to be anti-proliferative and pro-inflammatory.[87] Within the IRF1 targets, notably *IFIT3*,
540 *IFIT5*, and *OAS2*, known as IFN-response genes, we found clear associations between RNA
541 expression (RNA cluster 5) and chromatin accessibility near TSS (+/- 3Kb) as well as in
542 potential regulatory regions (+/- 50kB from TSS) in ATAC cluster 8 (**Fig. 6E**). These data
543 support cells in RNA cluster 5 have permissive chromatin that underlies persistent activation
544 of IFN-responses via IRF1.

545 The pseudotime analysis predicts RNA cluster 2 was most closely related, and strongly
546 interacted with RNA cluster 5 based on ligand-receptor inference, so we next examined if a
547 similar gene expression and chromatin accessibility could be identified in both clusters.

548 Some overlapping genes were found in cluster 2 with similar changes in nearby chromatin
549 accessibility and included inflammatory genes *HAX1* and *SERPINH1* (**Fig. 6E**). Grouped
550 clusters 0, 1, 3 exhibited little expression of *IRF1* target genes. GSEA on shared ATAC
551 signatures, both for gain and loss of accessibility suggested that common gain of accessible
552 regions were associated with stress response and blood brain barrier (BBB) maintenance,

553 whereas loss of accessible sites correlates with notch and BMP signaling, and senescence
554 pertaining to cell proliferation (**Fig. S5I-J**). This downregulation in notch and BMP signaling in
555 cluster 2, based on interactions with cluster 5, was also predicted from the ligand-receptor
556 interaction analysis (**Fig. 5K**). Importantly, not all changes in chromatin accessibility correlate
557 directly to variation in mRNA (**Fig. S5J**).

558 To further understand patterns based on chromatin accessibility and RNA expression, we
559 subdivided gene sets based on RNA upregulation in RNA clusters 0, 1, 3, and depletion in
560 RNA clusters 2 and 5, and found enrichment for terms pertaining to Wnt signaling and NSC
561 maintenance (**Fig. 6F**). We also found increased accessibility near the TSS of the RNA cluster
562 5 upregulated genes, again suggesting aberrant permissive chromatin in these cells allowing
563 for increased expression. When assessing coordinated upregulation of gene expression in
564 RNA clusters 2 and 5, we found enrichment in terms associated with mitochondrial
565 transmembrane transport, protein import, and telomerase RNA localization (**Fig. 6F**). These
566 results support a close interaction between RNA clusters 2 and 5, with cluster 5 being
567 specifically IFN-responsive.

568 Lastly, we inferred single-cell regulatory networks using SCENIC[88]. We observed that RNA
569 cluster 5 was defined by two major regulons, *IRF1* and *FOXP2*, that was associated with
570 genes regulating TNF and IFN signaling, as well as the p16-cyclin complex related to
571 senescence (**Fig. 6F, Table S9**). *PAX6* was also identified as a major regulon across all
572 clusters of the iNSCs and was defined by genes associated with nervous system
573 development, supporting their RG-like state. Overall, RNA cluster 5, primarily represented in
574 PMS iNSCs, is consistently defined by gene regulatory patterns that are associated with an
575 IFN-responsive and senescence state.

576 In summary, our work demonstrates that direct reprogramming technology maintains
577 hallmarks of PMS in cells due to maintenance of epigenetic memory. We reveal that patient
578 fibroblasts have hypomethylation at genes associated with lipid metabolic processes and IFN
579 signaling, which then became further accentuated upon direct induction into iNSCs.

580 Within the heterogeneous PMS iNSCs, we identify a novel disease associated cluster of
581 IFN-responsive, inflammatory RG-like cells that display senescent features and are regulated
582 by IRF1, which may spread dysfunctional features towards other clusters through their
583 secreted factors.

584 Integration with publicly available datasets further identifies and highlights a long-neglected
585 non-neurogenic DARG population, which is found significantly increased in chronic active
586 lesions areas and display IFN and senescence gene expression.

587

DISCUSSION

PMS is a complex neuroinflammatory and neurodegenerative disease that results from the interaction between environmental factors and genetic predisposition. The majority of genetic risk factors that have been identified in the development and progression of MS are associated with the peripheral immune system, mapping mainly to T cells, however recent work has also uncovered variants in genes expressed by glial cells.[89,90] MS severity has also been linked to variants involved in mitochondrial function, synaptic plasticity, and cellular senescence in genes expressed in the CNS.[18] To further understand how intrinsic glial cell dysfunction in PMS contributes to disease pathology we generated directly reprogrammed iNSCs.

Characterization of directly reprogrammed iNSCs showed PMS donor-derived cells reproduced reported phenotypes of increased expression of inflammatory signaling and senescence associated mRNAs compared to Ctrl cells.[17] Further, patient iNSCs maintained shorter telomere lengths compared to controls, indicating this type of reprogramming better maintains features of the donor cells that may be critical in driving the PMS phenotypes. We then established that iNSCs also maintained epigenetic signatures, as determined by DNA methylation age, after reprogramming from fibroblasts, indicating that this method of cellular reprogramming may conserve epigenetic information important for disease phenotypes. Globally, cell lines derived from people with PMS were found to have lower levels of DNA methylation, with enrichment of hypomethylation at promoter regions of targets for inflammatory transcription factors, such as STAT6 and NFκB. Interestingly, global hypomethylation has been identified to occur with aging in various organs in both mice and humans, which is believed to contribute to genome instability .[91]

Concordantly, hypomethylated regions in the PMS fibroblasts and iNSCs were enriched for pathways involved in immune response, suggesting global aberrant epigenetic regulation in individuals with the disease. Previous work has characterized global methylation signatures in the whole blood of people with MS and identified that half of the differentially methylated positions mapped to genes enriched in CNS cells and pathways.[92] This work identified neurodegenerative-related pathways as epigenetically dysregulated in severe MS cases, which correlated with acceleration of methylation age.[92] Intriguingly, we also characterize a loss of methylation in genes that regulate lipid metabolism, implicated in Ionescu, Nicaise et al.[46] Given these pathways appear to be highly relevant to PMS phenotypes, we believe human iNSC methodologies provides an excellent, and biologically valuable, platform for studying mechanisms driving disease.

Combined single-cell and single-nucleus RNA data analysis allowed us to better classify heterogenous iNSCs. Here we identified cells with both neural and RG phenotypes, and

importantly were able to find cells with matching transcriptional profiles from datasets generated from post-mortem MS brains. We found that most of the cell clusters were identified by mRNAs transcribed from radial glial genes (*SOX2*, *PAX6*), with one cluster which we identified with a neural progenitor mRNA signature (*DCX*, *ASCL1*). Within these clusters, we define a novel subset of cells that is predominantly composed of cells derived from PMS donor fibroblasts. This unique RNA cluster 5 displays an inflammatory phenotype expressing many features of senescence and interferon signaling and response.

The mechanisms underlying senescence and IFN signaling are intertwined. IFN response can be triggered by a myriad of stimuli, including extra and intracellular double-stranded (ds) RNA and DNA from cell stress and apoptosis, cytosolic DNA, viruses, and microbes, which in turn activates a pro-inflammatory response.[93] Over the course of aging, IFN pathways have been found to become aberrantly activated, which leads to global inflammation (*inflammaging*) and senescence.[94] The presence of an IFN signature in brain cells is increasingly being associated with aging and neurodegenerative diseases in rodent models and humans.[95-98] Type I IFN signatures are found upregulated in the aged brain, especially the choroid plexus, and in neurodegenerative diseases, where it may lead to recruitment and activation of immune cells and eventual neurodegeneration. Interestingly, in our model system, we identify hypomethylation of genes associated with IFN signaling in PMS fibroblasts, indicating a potential predisposition for developing an IFN response in people with PMS. Once fibroblasts are reprogrammed to iNSCs, they take on an even more pronounced IFN phenotype associated with senescence gene expression.

From the single-cell data, we establish not only the heterogeneity of iNSCs derived from both Ctrl and PMS donors, but also define a novel subset of disease associated RG-like cells that could be the 'drivers' of the inflammatory signature seen in the analysis of bulk PMS iNSCs. In fact, through ligand/receptor predicted interactions, the secretory factors from this – PMS mostly – IFN-responsive and senescent-like RNA cluster 5, could induce inflammatory-associated signatures (*i.e., neurodegeneration, oxidative stress induced senescence, and signaling by Ils*) and inhibit NSC maintenance (*i.e., Wnt signaling, and cell cycle*) in the other iNSC clusters, thus suggesting that RNA cluster 5 can further affect surrounding cells via amplification of such inflammation. Independent work from our group, further supports a key role for disease associated paracrine factors in conditioned iNSC media to induce neurite retraction and neuronal apoptosis.[46]

While the mechanisms of this RG-intrinsic intrinsic dysfunctional phenotype in PMS are still unknown, however, we do find epigenetic signatures starting even with the donor fibroblasts. Recently, neurodegenerative diseases have been found to be highly associated with viral exposure,[99] and in the case of MS the Epstein Barr virus (EBV) increases risk of disease.[100]

659 Viral exposure combined with chronic inflammation in PMS may induce global epigenetic
660 changes, affecting cells such as fibroblasts, found to be stressed in people with MS.[101]
661 Furthermore, the activation of human endogenous retroviruses (HERVs) in unique cell
662 populations are also associated with chronic inflammatory neurodegenerative diseases[102] and
663 brain injuries.[103] HERVs can be activated via inflammatory stimuli and induce an IFN response,
664 similar to that of a viral infection.

665 Epigenetically, we identify sites with gains of accessibility are associated with IFN-response
666 and signaling as well as cytokine production in RNA cluster 5 (corresponding to ATAC cluster
667 8) composed mainly of PMS derived cells. The epigenetic remodeling in this cluster was also
668 associated with increased accessibility at binding sites of the p53 motif, known to be activated
669 in response to cellular stress and DNA damage and promotes sustained IFN signaling and
670 response.[85]

671 Using publicly available datasets generated from MS post-mortem brains,, we assessed
672 the expression of RG genes and identified non-neurogenic RG-like cells within well-known
673 astrocyte clusters. Recent work has demonstrated that astrocytes exhibit plasticity in injury
674 situations.[41] Human pathologies which involved lesions and blood-brain barrier rupture were
675 associated with a de-differentiation of astrocytes to replicating NSC/RG-like cells.[41]
676 Furthermore, this has been previously validated in rodent models where epithelial injury allows
677 for neural precursors to dedifferentiate into multipotent NSCs in the olfactory epithelium.[104]
678 Based on these studies, astrocytes in PMS may be undergoing (i) a de-differentiation (or de-
679 maturation) process, where they begin to express cell cycle and early RG-like cell markers
680 due to exposure of chronic inflammation, and a (ii) resurgence as non-neurogenic RG-like
681 cells at the level of disease-associated, ectopic, non-canonical niches.

682 Integration of our in vitro iNSC data with publicly available datasets in fact identifies and
683 highlights a long-neglected, non-neurogenic disease-associated RG-like cell population, being
684 found significantly increased in chronic active lesions areas and displaying IFN and
685 senescence gene expression, which we term DARGs.

686 Interestingly, we identify twice as many DARGs in chronic active PMS lesions, which are
687 slowly expanding in nature, feature smouldering inflammatory demyelination at the edge,
688 remyelination failure, and axonal degeneration,[105] and are associated with a more aggressive
689 disease[106]. Further characterization of the phenotype of this novel DARG population showed
690 increased expression of the SenMayo and IFN-associated genes compared to the astrocyte
691 cluster.

692 Overall, our work shows there are epigenetic alterations in somatic fibroblasts isolated from
693 people with PMS, and many of these epigenetic modifications remain following direct

694 reprogramming into iNSCs. These epigenetic alterations are associated with de-repression
695 (hypomethylation and increased chromatin accessibility) of IFN signaling and response as well
696 as inflammation. We further uncover a novel subset of PMS iNSCs with high levels of
697 inflammatory signaling, which we propose drives much of the bulk phenotype.

698 Lastly, we uncover a long neglected DARG population in the PMS brain, which has similar
699 mRNA profiles as the *in vitro* PMS iNSCs, including expression of senescence and IFN
700 transcripts.

701 Our research lays the groundwork for further investigating 'disease-pacemaker' non-
702 neurogenic RG-like cells in potentially driving neuroinflammation in neurodegenerative
703 disease. Future work is needed to identify the origin and driver of epigenetic dysfunction
704 arising in the cells of people with PMS.

705
706
707

708 LIMITATIONS OF STUDY

709 While we generated cell lines from individuals with PMS, the variations in genetic
710 backgrounds, sex, and age among these lines pose a potential limitation. Despite our thorough
711 analysis of both patient and control cell lines, we acknowledge the necessity for additional
712 validation of our findings in situ. Additionally, the inclusion of induced pluripotent stem cells
713 (iPSCs) from the same donors would have enhanced the data quality, allowing for a more
714 robust interrogation of the observed cellular phenomena. Utilizing single-cell spatial biology
715 methodologies could offer a more comprehensive understanding of our results, particularly in
716 capturing differences related to disease-relevant microenvironments and surrounding cells
717 (neighbors).

718
719
720

721 ACKNOWLEDGMENTS

722 The authors wish to acknowledge L. Bonfanti, A. D'Alessandro, V. Fossati, D. Franciotta, C.
723 Frezza, O. Hruba, G. Pluchino, A. Quaegebeur, S. Rizzi, L. Roth and A. Speed for technical
724 and intellectual inputs throughout this study.
725 This research was supported by the Ferblanc Foundation G112716 (SP and AMN); Catalyst
726 Award from the UK MS Society H160 (SP and CMW); National MS Society Research Grant
727 RG 1802-30200 (SP and LPJ); Bascule Charitable Trust RG98181 (SP); Wings for Life RG

82921 (SP and LPJ), and the Fondazione Italiana Sclerosi Multipla FIMS 2018/R/14 (SP and LPJ) and 2022/R-Single/011 (SP).
BP, DT, JW, LC, JL, JF, SD, MG, and IB are supported by the Intramural Research Program of the National Institute on Aging. AMN is the recipient of a European Committee for Treatment and Research in Multiple Sclerosis (ECTRIMS) Postdoctoral Research Fellowship Exchange Program fellowship (G104956) and is supported through a UK MS Society Centre Excellence grant (G118541). PP is supported through an MRC-DTP and Cambridge Trust PhD studentship and consumable award (RG86932) and Queen's College Tutorial Award. RBI is supported through an MRC-DTP and Cambridge Trust studentship and consumable award (RG86932) and St. Edmund's College Tutorial Award. CW is supported through a National MS Society Post-doctoral fellowship (FG-2008-36954). LPJ was supported by a Fondazione Italiana Sclerosi Multipla FIMS and Italian Multiple Sclerosis Association AISM Senior research fellowship financed or co financed with the '5 per mille' public funding cod. 2017/B/5 (LPJ), a Wellcome Trust Clinical Research Career Development Fellowship (G105713), and a National MS Society Research Grant RFA-2203-39318. FE was supported by the Austrian Science Fund FWF (FWF-INTER – INTER/FWF/19/14117540/Pdage and the SFB F78 "Neuro Stem Modulation", SFB F7810-B). IM is supported by Wellcome Trust (203151/Z/16/Z) and the UKRI Medical Research Council (MC_PC_17230).

AUTHOR CONTRIBUTIONS

Conceptualization, BP, AMN, DT, IM, SP, IB; Methodology, BP, AMN, DT, JW, LC, JL, RBI, JF, SD, MSC, TL; Investigation, BP, AMN, DT, LP, MLDN, PP, JW, LC, JL, RBI, CMW, GK, JF, SD, MSC, TL, FE, MG, IM, SP, IB; Writing – Original Draft, BP, AMN, DT; Writing – Review & Editing, AMN, IM, SP, IB; Funding Acquisition, AMN, CMW, LPJ, IM, SP, IB; Resources, JF, SD, TL, AS, FE; MG; Supervision, MG, IM, IM, SP, IB.

DECLARATION OF INTERESTS

SP is founder, CSO and shareholder (>5%) of CITC Ltd and Chair of the Scientific Advisory Board at ReNeuron plc. The other authors declare that they have no competing interests.

FIGURE LEGENDS

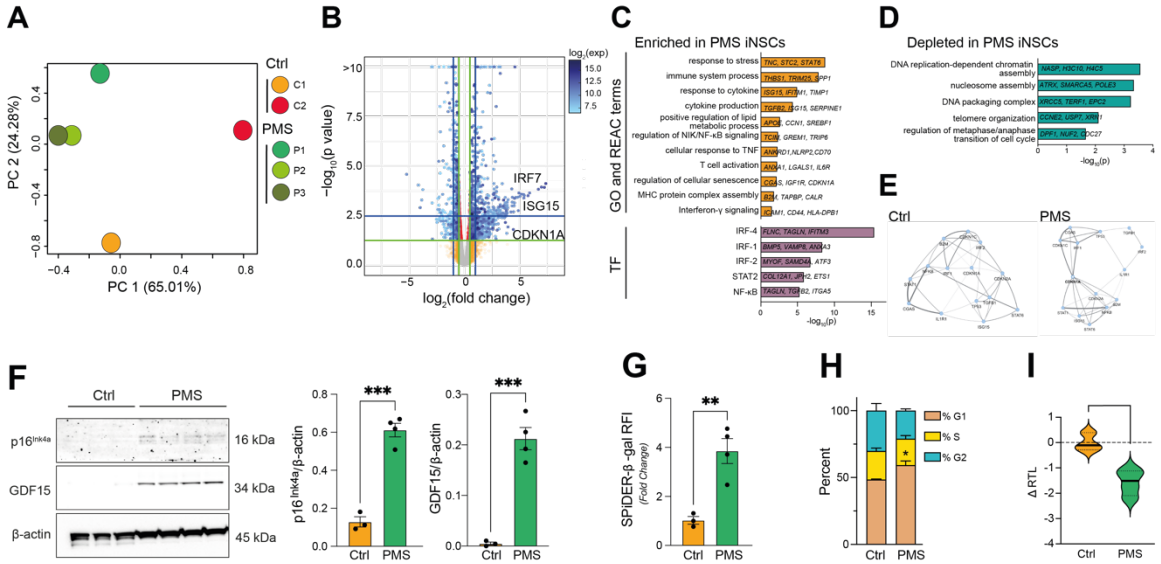

Figure 1. Bulk mRNAseq reveals increased inflammatory signaling and senescence markers in PMS iNSCs.

(**A**) PCA summarizing the co-variation of expression levels in the bulk RNA sequencing. C and P are independent cell lines.

(**B**) Volcano plot illustrating differentially expressed transcripts, *vs* $\log_2$ abundance in PMS iNSCs compared to Ctrl iNSCs. Log_2(FC) *vs* adjusted p-values (with Benjamini Hochberg multiple testing correction) are reported.

(**C-D**) Pathway enrichment analysis on GO and REAC terms and enriched transcription factors (TF) based on TransfFac annotation, from bulk mRNA sequencing.

(**E**) Gene regulatory networks, inferred on manually curated, differentially expressed transcripts contrasting of Ctrl *vs* PMS iNSCs networks, derived from the bulk mRNA sequencing.

(**F**) Representative western blots and quantification for $p16^{Ink4a}$, GDF15, and β-actin.

(**G**) Quantification of relative fluorescence intensity (RFI) of senescence-associated β-galactosidase expression using SPiDER-β-gal. Data represented as a fold change over Ctrl iNSCs.

(**H**) Flow cytometry-based quantification of iNSC cell cycle states. Data plotted as cells in percent of cell cycle state.

(**I**) Quantification of changes in PMS relative telomere length (RTL) over Ctrl iNSCs.

Experiments in **F-I** were done on n= 3 Ctrl and n= 4 PMS iNSC lines each performed in n= 3 replicates. Data in **F-I** are mean values ± SEM. *$p \leq 0.05$, **$p \leq 0.01$, ***$p \leq 0.001$, un-paired t-test, with unequal variances.

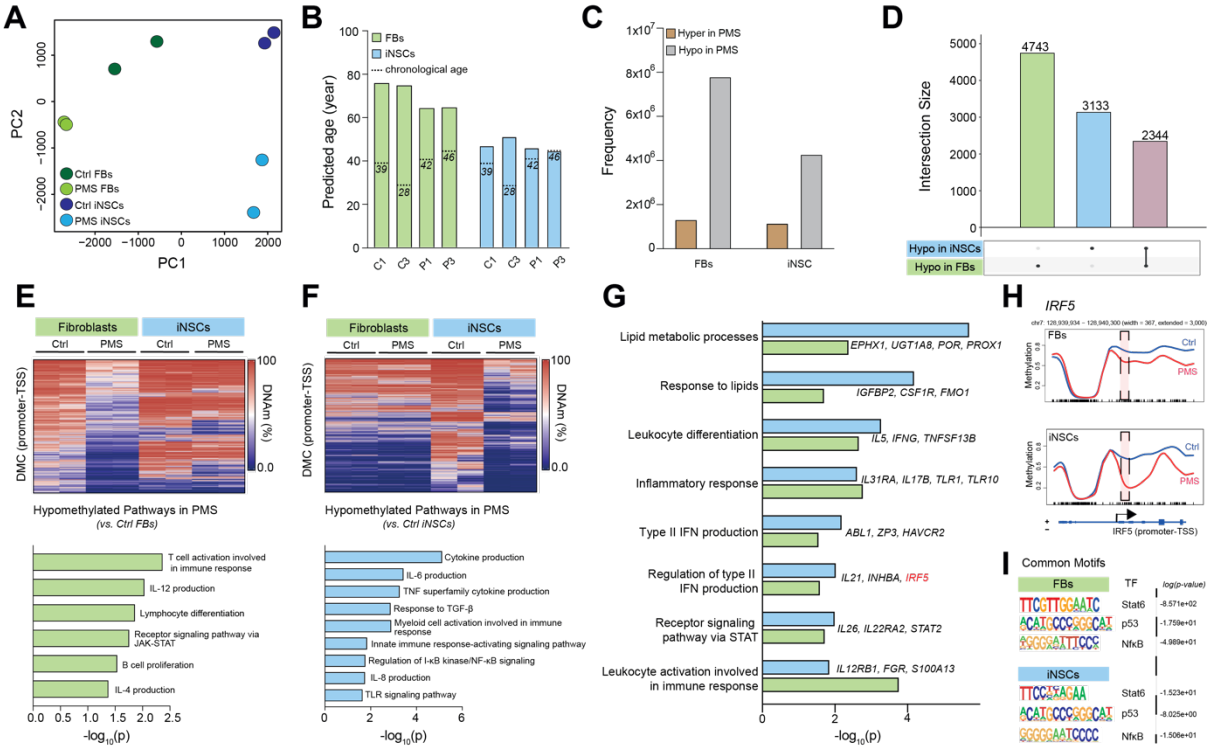

Figure 2. Whole genome bisulfite sequencing (WGBS) uncovers inflammatory pathways found commonly hypomethylated in PMS fibroblasts and iNSCs.

(**A**) PCA summarizing methylation quantified in the WGBS data for fibroblasts and iNSC samples.

(**B**) Cortex age DNA methylation aging clock inference. Dashed line indicates chronological age at which FBs samples were sampled.

(**C**) Frequency of differentially methylated cytosines (DMC), plotted as Ctrl *vs.* PMS.

(**D**) UpSet plot of hypomethylated genes within the promoter-transcription start site (TSS) region.

(**E-F**) Heatmap and enrichment analysis of hypomethylated genes.

(**G**) Enrichment analysis of commonly hypomethylated genes in PMS (*vs* Ctrl) fibroblasts (light green) and iNSCs (light blue).

(**H**) Example of methylation difference for *IRF5* (genome browser tracks), as in **G**.

(**I**) Proportional sequence logos on HOMER motifs resulting from an enrichment analysis from **E**.

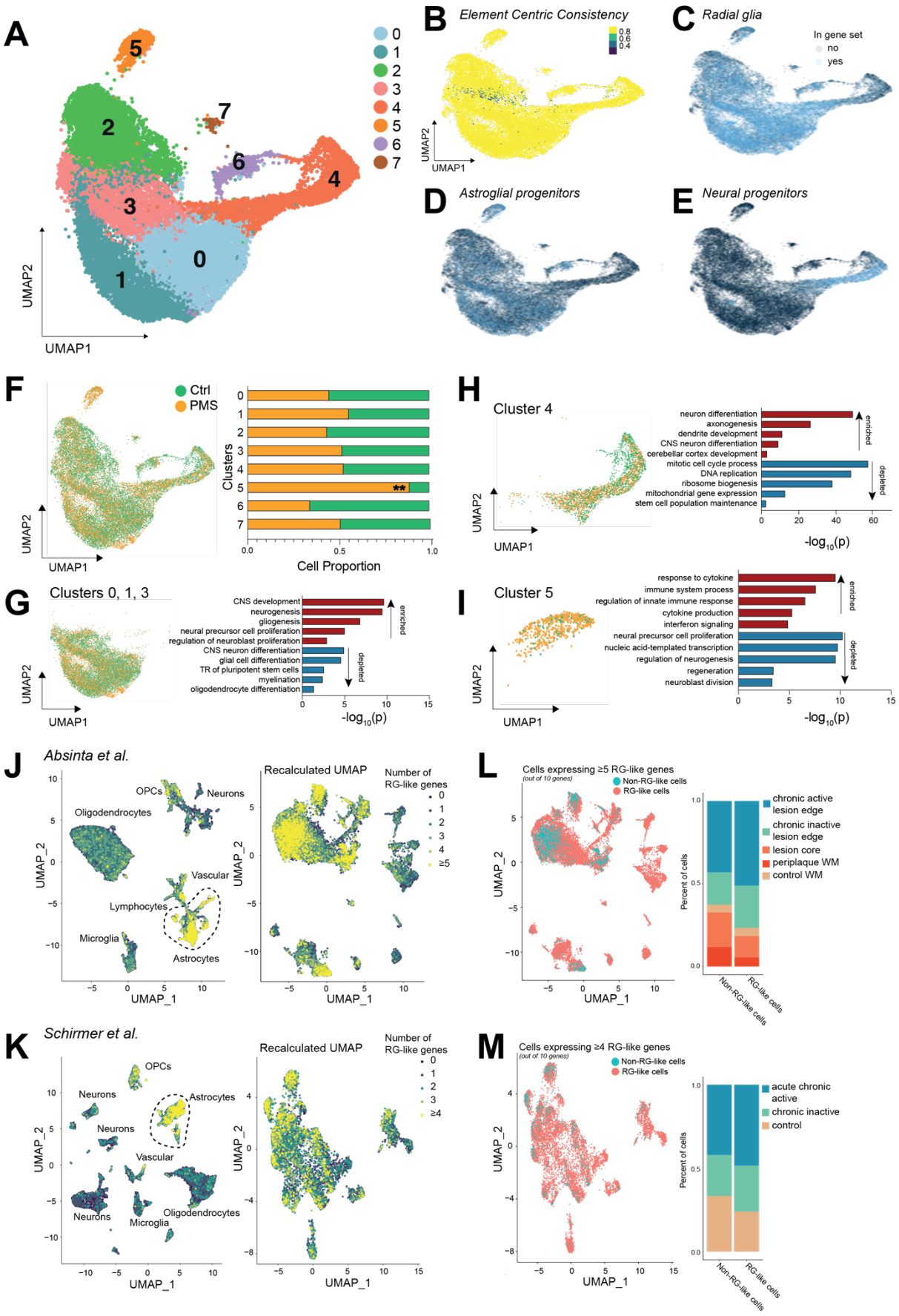
A
B Element Centric Consistency
C Radial glia
In gene set
no
yes
D Astroglial progenitors
E Neural progenitors
UMAP1
UMAP2
F
Ctrl
PMS
Clusters
Cell Proportion
H
Cluster 4
neuron differentiation
axonogenesis
dendrite development
CNS neuron differentiation
cerebellar cortex development
mitotic cell cycle process
DNA replication
ribosome biogenesis
mitochondrial gene expression
stem cell population maintenance
enriched
depleted
-log10(p)
G
Clusters 0, 1, 3
CNS development
neurogenesis
gliogenesis
neural precursor cell proliferation
regulation of neuroblast proliferation
CNS neuron differentiation
glial cell differentiation
TR of pluripotent stem cells
myelination
oligodendrocyte differentiation
I
Cluster 5
response to cytokine
immune system process
regulation of innate immune response
cytokine production
interferon signaling
neural precursor cell proliferation
nucleic acid-templated transcription
regulation of neurogenesis
regeneration
neuroblast division
J Absinta et al.
OPCs
Neurons
Oligodendrocytes
Vascular
Lymphocytes
Microglia
Astrocytes
Recalculated UMAP
Number of RG-like genes
UMAP_1
UMAP_2
L
Cells expressing ≥5 RG-like genes
(out of 10 genes)
Non-RG-like cells
RG-like cells
chronic active lesion edge
chronic inactive lesion edge
lesion core
periplaque WM
control WM
Percent of cells
K Schirmer et al.
M
Cells expressing ≥4 RG-like genes
acute chronic active
chronic inactive
control

804

Figure 3. iNSCs display a RG-like transcriptomic signature that can be identified in the adult human brain using single nuclei sequencing.

(**A**) UMAP of Ctrl and PMS iNSC single-cell, -nucleus RNAseq samples, post quality checking and filtering; a stable partitioning of cells is also highlighted.

(**B**) Element centric consistency, derived on 30 iterations, calculated per cell, and visualized on the RNA UMAP.

(**C-E**) Voting scheme of transcripts associated with a RG-like signature (**C**), astroglial progenitor signature (**D**), and neural progenitor signature (**E**) as in **A**.

(**F**) Cluster distribution in human iNSCs on the RNA UMAP. The histogram summarizes cell proportions per cluster. **$p \leq 1e\text{-}106$ (X^2 test).

(**G-I**) Enrichment analysis of enriched and depleted terms in clusters 0, 1, 3 (**G**); cluster 4 (**H**); cluster 5 (**I**) *vs* all other clusters; recalculated RNA UMAPs illustrating the distribution Ctrl *vs* PMS cells.

(**J-K**) Recalculated UMAPs of RG-like cells in two *ex vivo* MS datasets, *Absinta et al., 2021* (**J**) and *Schirmer et al., 2019* (**K**). OPCs, oligodendrocyte progenitor cells.

(**L-M**) Voting scheme UMAPs and histograms summarizing the frequency of RG-like cells (and non-RG-like cells per area of interest as in **J-K**. WM, white matter.

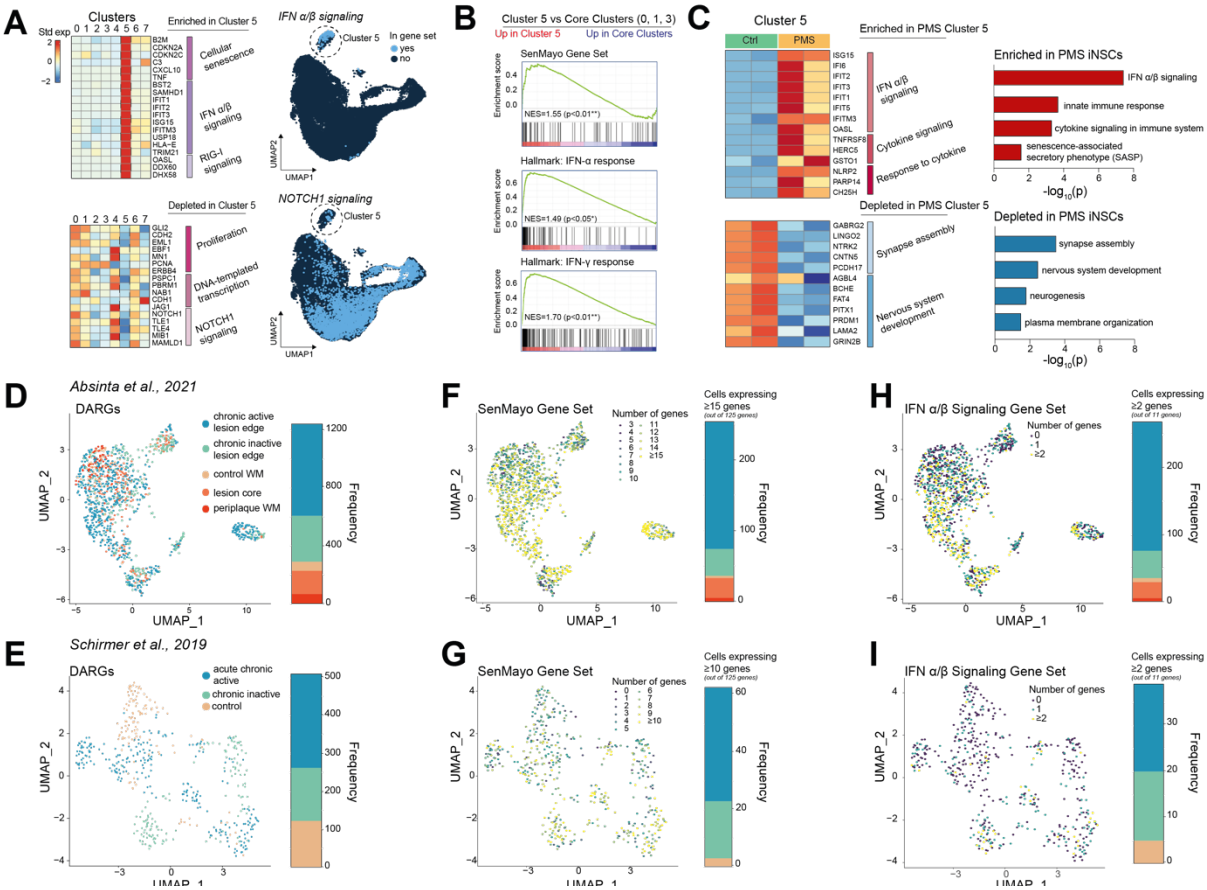

Figure 4. A specific PMS iNSC cluster displays senescence and IFN-signaling which is also identified in DARGs of the PMS brain.

(**A**) Heatmap of RNA cluster 5 signature genes and summary of associated enrichment terms. Voting scheme UMAP of genes associated with IFN- α/β signaling and NOTCH1 signaling.

(**B**) Enrichment plots of the SenMayo gene set, and the IFN-α, and IFN- γ response in cluster 5.

(**C**) Heatmap of standardized expression of highly expressed *vs* depleted genes, specific to only PMS cells *vs* Ctrl cells in RNA cluster 5 and selected enriched pathways significant for the selected genes.

(**D-E**) Recalculated UMAP on the filtered cells identified as DARGs in **Figure 3L-M**. Stacked Histograms summarizing the frequency of cells per lesion area.

(**F-I**) UMAPs and histograms of DARG frequency that express genes in the SenMayo gene set and IFN- α/β signaling gene set respectively, from *Absinta et al., 2021* and *Schirmer et al., 2019* data.

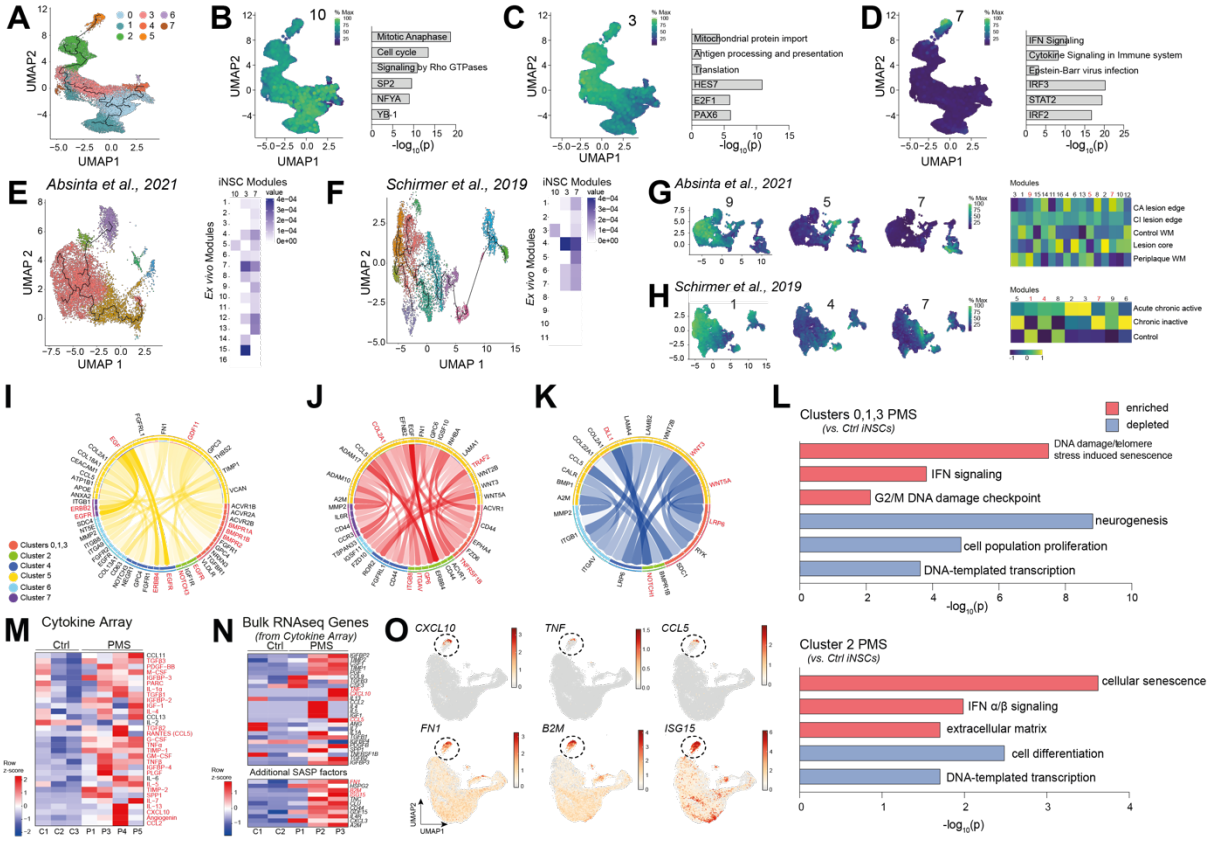

Figure 5. PMS iNSCs secrete a pro-inflammatory SASP that induces upregulation of genes associated with inflammation and senescence.

(**A**) Pseudotime trajectory inferred and displayed on the *in vitro* dataset UMAP. Cluster 5 was used as initialization point (*endpoint*).

(**B-D**) UMAP of the distribution of intensity of genes clustered in modules 10 (**B**), 3 (**C**), and 7 (**D**), determined based on the pseudotime ordering. GSEA summary and TFs corresponding to gene modules 10 (**B**), 3 (**C**), and 7 (**D**).

(**E-F**) UMAP of pseudotime trajectory inferred from the *Absinta et al., 2021* (**E**) and *Schirmer et al., 2021* (**F**) datasets, respectively. The heatmaps summarize the scaled proportions of common genes matching between iNSC *in vitro* modules 10, 3, and 7 with *ex vivo* modules.

(**G-H**) Modules selected from the *ex vivo* datasets as in **E-F** recapitulating the manually curated modules (**B-D**) identified on the *in vitro* pseudotime trajectory. The heatmaps summarize the scaled averaged expression of the *in vitro* gene modules, projected on the *ex vivo* datasets.

(**I-K**) Circos plots of the intercellular ligand-receptor interactions predicted using NicheNet. (**I**) Yellow directed edges indicate interactions, (**J**) red edges summarize enriched ligand/receptor interactions i.e. upregulated target genes, (**K**) blue edges summarize depleted ligand/receptor interactions i.e. downregulated target genes, between cluster 5 and complement clusters in Ctrl and PMS iNSCs.

(**L**) Enrichment summary on enriched and depleted genes in clusters 0,1,3 and cluster 2 (Ctrl *vs* PMS).

(**M**) Heatmap of cytokine array performed on CM. Color intensities are proportional with standardized normalized intensities. Proteins investigated also in the mRNAseq (**N**) are highlighted in red.

(**N**) Heatmap of standardized normalized expression levels of genes coding for secreted proteins as in **M**. Genes investigated also in the single cell data (**O**) are highlighted in red.

(**O**) Expression gradient UMAPs of the selected secreted proteins as genes (**N**).

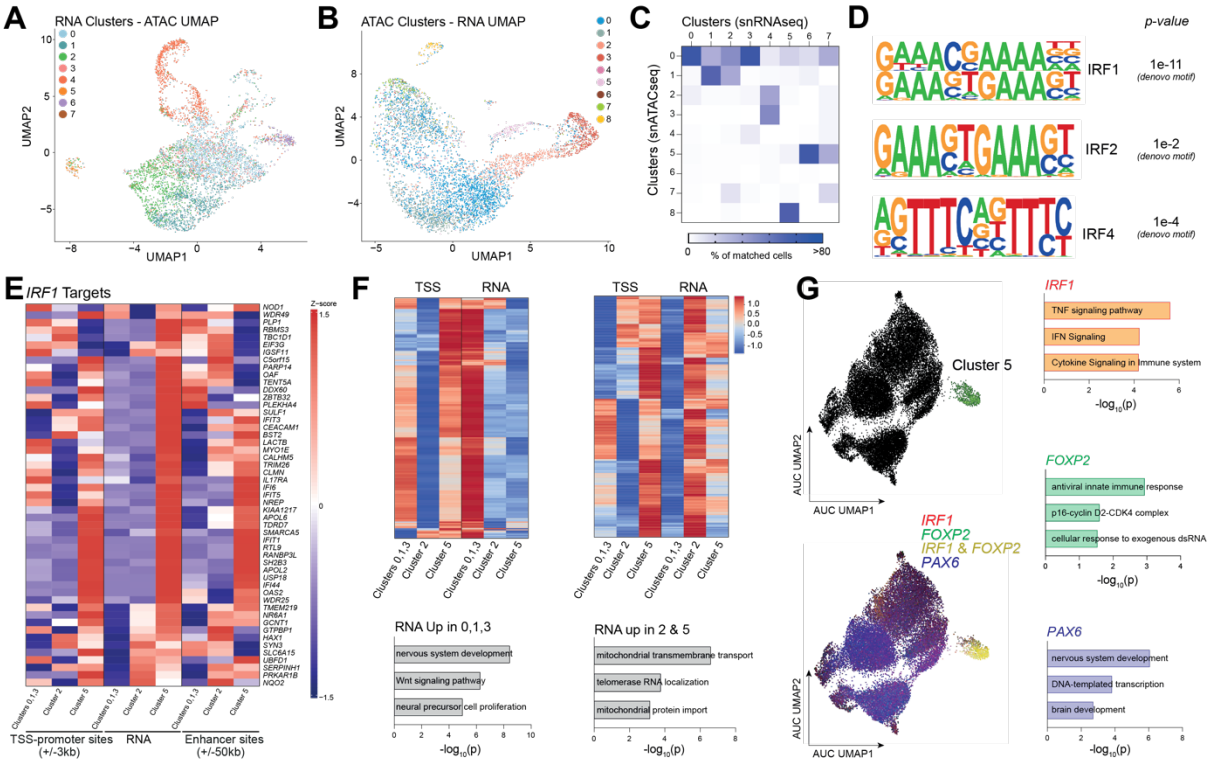

Figure 6. Multi-omics RNA/ATAC integration with further epigenetic characterization of cluster 5 cells.

(**A**) ATAC UMAP of the overlaid localization of RNAseq clusters.

(**B**) RNA UMAP of the overlaid localization of snATACseq clusters.

(**C**) Heatmap of the percentage of matched assignations of cells across the snRNAseq and snATACseq clusters. The analysis was performed solely on matched cells i.e. cells with both RNA and ATAC expression.

(**D**) Enriched motifs of signature and differentially accessible genes identified on the RNA cluster 5, and ATAC cluster 8.

(**E**) Heatmap of accessibility (ATAC) and expression (RNA) of *IRF1* targets, i.e. TSS, RNA, and distal portions of marker genes identified as differentially expressed between grouped RNA clusters 0, 1, 3 *vs* cluster 2, and cluster 5, respectively.

(**F**) Heatmap of marker genes, between clusters 0, 1, 3 *vs* 2 and 5. The summary of enrichment analysis applied on the selected genes.

(**G**) SCENIC GRN inference summary and selection of IRF1 specific regulons, corroborated with enrichment analysis of regulons (*IRF1*, *FOXP2*, *PAX6*). The GRN inference was performed on the scRNAseq dataset.

METHODS

Data and code availability

All codes used in the study are available on github: https://github.com/Core-Bioinformatics/DARG_PMS

- Any additional information required to reanalyze the data reported in this paper is available from the lead contacts upon request.
- All data generated for this study, in raw and processed format, are publicly available on the Gene Expression Omnibus (GEO), under accessions GSE243319, GSE251839, GSE251831, GSE251838, and GSE251830. Further data mining of processed data may be performed on bulkAnalyseR for bulk sequencing datasets and ClustAssess and Shiny Cell apps (https://bioinf.stemcells.cam.ac.uk/shiny/pluchino/DARG_PMS/bulkanalyser/, https://genomicspark.shinyapps.io/shinyApp/) for single-cell/ nuclei datasets. UCSC genome browser sessions for these datasets comprise: https://genome-euro.ucsc.edu/s/CSCI/DARG_PMS and http://tinyurl.com/2ygsa6or.

EXPERIMENTAL MODEL AND SUBJECT DETAILS

Patient cells

The cohort consists of 5 PMS and 3 healthy controls between 25 and 63 years of age. The cohort includes representation from both genders, distributed across PMS and control groups (Table S1). PMS fibroblasts were provided by the New York Stem Cell Foundation (NYSCF) Research Institute through their Repository (http://www.nyscf.org/repository)[107]. Patients were recruited at the Tisch Multiple Sclerosis Research Center of New York, upon informed consent and institutional review board approval (BRANY). PMS donors underwent clinical assessment when recruited for the study. Control fibroblasts C1 and C2 (Table S1) were generated from adult dermal fibroblasts after obtaining consent and ethical clearance by the ethics committee of the University of Würzburg, Germany.

Generation and culturing of induced neural stem cells

iNSC lines were generated and quality controlled as described in *Ionescu, Nicaise et al.*[46] and *Meyer et al.*[45] iNSCs were maintained in neural induction media (NIM) consisting of DMEM/F12 and Neurobasal (1:1) (ThermoFisher), supplemented with N2 supplement (1x) (ThermoFisher), 1% glutamax (ThermoFisher), B27 supplement (1x) (ThermoFisher), CHIR99021 (3 μM) (Cell Guidance Systems), SB-431542 (2 μM) (Cayman Chemical), and hLIF (10 ng/ml) (PeproTech) until 70% confluent, then lifted using accutase, spun at 300 x g for 3 mins, and plated onto growth factor reduced (GFR) matrigel matrix coated plates

922 (Corning) (1:20 in DMEM/F12) with Y-27632 (10 μM) (Miltenyi Biotec) between 1:3-1:5 in NIM
923 media. Media was changed every second day as needed. Experiments were performed on
924 cells from passages 20-35.
925
926 *Fibroblast maintenance*
927 Fibroblasts were maintained in growth medium (DMEM Glutamax I [Thermo Fisher])
928 supplemented with 10% fetal bovine serum, 1% non-essential amino acids and 1 mM sodium
929 pyruvate (ThermoFisher) at 37°C with 5% CO_2 and fed every 3-4 days. After reaching 90%
930 confluency the fibroblasts were detached with trypsin-EDTA 0.05% for 5 min followed by
931 neutralization in DMEM and spun down at 300xg for 5 min. They were split 1:4 into growth
932 media onto tissue-culture treated plasticware.
933
934
935 **METHOD DETAILS**
936 *mRNA sequencing, analysis, and inference of Gene Regulatory Networks (GRNs)*
937 iNSC lines, between passages 15-30, were plated at 500,000 cells per well in GFR-coated 6-
938 well plates. After 24 hours, the media was refreshed with new NIM. Cells were harvested in
939 RLT lysis buffer 72 hours after plating then frozen at -80°C until extraction. RNA extraction
940 was performed according to standard steps described for the RNeasy kit, followed by DNase
941 treatment (Qiagen). RNA was quantified using the NanoDrop 2000c instrument. Illumina
942 Sequencing libraries were prepared using the TruSeq low sample protocol from 1 μg of total
943 RNA (Illumina, San Diego, CA, USA). The resulting libraries were sequenced in paired-end
944 mode, on 150 nts reads on an Illumina NovaSeq 6000 instrument.
945 The quality checking of the samples was assessed using fastQC v0.12.11, applied on raw
946 files; the outputs were summarised using multiQC 1.14.[108] Initial sequencing depths ranged
947 from 30M to 44M reads; subsampling without replacement, done using seqtk 1.3-r106 [109], was
948 performed to 34M reads, to avoid inconsistencies caused by uneven sequencing depths.[110]
949 All samples were aligned to the GRCh38.p13 genome using STAR 2.7.10a (paired-end
950 mode).[111] Expression quantification was performed using featureCounts v.1.6.3.[112] The
951 distribution of signal across transcripts was assessed on the UCSC genome browser. The
952 tracks (bigwig format) were built from the bam files using samtools 1.17.[113] Next, noisyR 1.0.0[48]
953 was used to estimate and remove noise from the count matrix; the raw expression levels were
954 normalised using quantile normalisation.[114] Differentially expressed genes (DEGs) were
955 identified using edgeR[50] and DESeq2[49]; due to the noise correction the DEG calling
956 converged; p-values were adjusted using Benjamini-Hochberg multiple testing correction.

bulkAnalyseR 1.1.0[47] was used to build a shareable interface for the analysis and visualisation of data.

The Gene Regulatory Networks (GRNs) were predicted, and their dynamics assessed, on the bulk RNAseq data using a bulkAnalyseR ShinyApp.[47] Additional analyses were performed using GENIE3[115] and visNetwork[116] to visualise subgraphs according to selected pathways and a maximum of 30 edges. To assess the global trend in co-variation of expression, for genes annotated to the selected pathways, density plots were created, per pathway, on the weights of the edges in the larger GRNs (corresponding values in the global adjacency matrix).

Immunoblotting

iNSCs were homogenized in 10X RIPA buffer (Abcam) supplemented with 100X protease and phosphatase inhibitors (ThermoFisher). Protein concentration was assessed using a BCA assay (ThermoFisher). Equal protein amounts (25 µg) were resolved by SDS-PAGE on Bolt™ Bis-Tris Plus pre-cast 4-12% gradient gels (Invitrogen) and transferred to 0.45 mM polyvinylidene fluoride (PVDF) membranes (Thermo Scientific). Membranes were blocked with TBS blocking buffer (LI-COR Biosciences) and immunoblotted with the indicated antibodies: mouse anti-p16^{Ink4a} (Invitrogen) at 1:500, rabbit anti-GDF15 (Proteintech) at 1:1000, and mouse anti-b-actin (Sigma) at 1:5000 in TBS blocking buffer (LI-COR Biosciences) with 0.1% Tween, followed by fluorescent secondary antibodies IRDye 680RD Goat anti-Rabbit or IRDye 800CW Goat anti-Mouse (LI-COR Biosciences) at 1:10,000 in TBS blocking buffer (LI-COR Biosciences) with 0.1% Tween and 0.01% SDS. The immunoblots were visualized with the ChemiDoc MP Imaging system (Bio-Rad). Densitometric analysis was conducted with Fiji by ImageJ. Protein targets were normalized to β-actin.

SPiDER-gal

Cells were plated on black-walled, clear bottom 96-well plates (ThermoFisher, 165305) at 15,000 cells/well and maintained in culture for 5 days. Expression of senescence associated β-galactosidase was measured by a SPiDER-b-gal-based cellular senescence plate assay kit (Dojindo) according to manufacturer's instructions. Briefly, cells were washed with PBS, stained with 1 µg/mL Hoechst (Sigma-Aldrich) as a measure of cell number, washed again, before the fluorescence intensity was measured at 358nmEx/461nmEm. Cells were then lysed with the provided buffer and the SPiDER-b-gal stain was added and incubated at 37°C overnight. Fluorescence intensity was measured at 520ex/565em. The SPiDER-b-gal fluorescence intensity of each well was corrected for the autofluorescence of empty wells and normalized to the Hoechst fluorescence intensity of the respective well to normalize for cell

993 number. The resulting average SPiDER-b-gal/Hoechst fluorescence intensity of each cell line
994 was normalized to that of healthy control cell lines.
995
996 *Cell Cycle Analysis*
997 iNSCs were plated at a density of 80,000 cells/cm^2 on GFR-coated plates. After 3 days cells
998 were lifted using accutase and then pelleted at 500 x g for 5 minutes. The cells were fixed in
999 70% ethanol for 30 minutes on ice then pelleted at 850 x g for 5 minutes. The cell pellet was
1000 resuspended in RNase (100 ug/mL) for 15 minutes and incubated at room temperature.
1001 Propidium iodide (1 ug/mL) was added to each sample and cells were analyzed on a BD
1002 LSRFortessa with the flow rate on slow. 20,000 events were collected for each sample. The
1003 data was analyzed using FlowJo 10.9 software using the Dean-Jett-Fox approach.
1004
1005 *Telomere length analysis*
1006 Relative telomere length was assessed using the Joglekar et al. protocol using quantitative
1007 PCR (qPCR) and comparison to that of a single copy gene.[117] iNSCs were plated at a density
1008 of 80,000 cells/cm^2 on GFR-coated plates. After 3 days cells were lifted using accutase and
1009 then pelleted at 500 x g for 5 minutes. DNA was isolated according to the DNeasy Blood &
1010 Tissue Kit (Qiagen) and quantified using the Nanodrop 2000c instrument. For initial
1011 optimization of the qPCR reaction, the DNA was diluted to three different concentrations (100
1012 ng/µL, 25 ng/µL, 6.25 ng/µL), and it was determined that 100 ng/uL had the best efficiency for
1013 both the human β-globulin and telomere primers. Two PCR reactions were separately
1014 conducted, for human β-globulin the mastermix was made using 5 µL Fast SYBR Green
1015 (ThermoFisher), 1 µL of hbg1 primer (3 µM), 1 µL of hbg2 primer (7 µM), and 2 µL of nuclease-
1016 free water. The reaction was cycled at 58°C annealing temperature along with a melt curve
1017 analysis using a QuantStudio 7 Flex (ThermoFisher). For the telomere primers, the mastermix
1018 was made using 5 µL Fast SYBR Green (ThermoFisher), 1 µL of telomere A primer (1 µM), 1
1019 µL of telomere B primer (3 µM), and 2 µL of nuclease-free water. The reaction was cycled at
1020 56°C annealing temperature along with a melt curve analysis using a QuantStudio 7 Flex
1021 (ThermoFisher). Each sample was run in duplicate. Average telomere length was calculated
1022 as the ΔΔCT = (PMS average hbg Ct – PMS average telomere Ct) – (Control hbg Ct – control
1023 average telomere Ct).
1024
1025 *Whole genome bisulfite sequencing (WGBS)*
1026 Genomic DNA was extracted from 100,000 fibroblasts and iNSCs using the DNeasy Blood
1027 and Tissue Kit (Qiagen). The quantity of DNA was measured using the Quant-iT PicoGreen
1028 method and victor X2 fluorometry (ThermoFisher), and the integrity of the DNA was evaluated
1029 with Agilent genomic DNA screen tape. 500 ng of genomic DNA was used for sequencing. The

1030 sample quality control criteria for the WGBS library were set to having a DNA integrity number
1031 (DIN) score of 7.0 and above. The extracted DNA was fragmented to an average insertion
1032 size of 550 base-pairs and the fragments were attached to end-repaired adapters. Genomic
1033 DNA was bisulfite converted using the EZ DNA methylation Gold kit (Zymo, Catalog #D5005)
1034 following the manufacturer's instructions. We next applied the xGen Methyl-Seq Lib Prep kit
1035 (Integrated DNA technologies, Catalog #10009824) to the prepare the genomic DNA library.
1036 Library quality control was performed using qPCR (LightCycler 480) and TapeStation 4200
1037 (D1000 screen tape).
1038 The dataset comprises 8 samples (4 fibroblast lines and 4 iNSC lines), with sequencing depths
1039 varying from 213M to 408M, and an average of 315M reads per sample. Reads with adapter
1040 contamination were trimmed using Trim Galore (0.4.3)[118] with options: --paired –q 25. Trimmed
1041 reads were aligned to the *H sapiens* reference genome (version hg38), using HISAT2[119]
1042 (version built in the current stable version of Bismark 0.23.1[120]). A bisulfite-converted index
1043 (GA and CT conversion) was generated with default parameters. We identified 28M CpG sites
1044 per sample, with sequencing coverage varying from 24x to 39x, (an average of 30x coverage
1045 per sample). The bismark_methylation_extractor tool was used to summarize the methylation
1046 levels at CpG sites. After assessing the bias at 5'end regions using M-bias results, the first
1047 2nts were excluded, as follows: bismark_methylation_extractor -p –ignore 2 –ignore_r2 –
1048 comprehensive –no overlap –bedGraph –counts –buffer_size 16G ($Aligned read bam file).
1049
1050 *Identification of differentially methylated sites and regions*
1051 MethylKit[121] was used for DMC and DMR quantifications, and fibroblast *vs* iNSC comparisons.
1052 A minimum threshold minimum of 10nts coverage for downstream DNA methylation analysis
1053 was set. The aligned reads were split into 100nt tiles (DMRs) using metilene.[122] Differential
1054 methylation was calculated, applying a McCullagh and Nelder[123] correction for overdispersion,
1055 as well as the sliding linear model (SLIM) proposed in methylKit to correct for multiple testing.
1056 Tiles with a q-value < 0.05 and over 20% methylation difference were called differentially
1057 methylated. Motif enrichment analysis was performed using Homer (*findMotifsGenome.pl*).
1058 Annotations relevant for the hg38 v6.4 of the *H sapiens* reference genome (genes, exons,
1059 introns, UTRs, and other annotations) were extracted using Homer annotation tools.
1060 AnnotatePeaks.pl DMR hg38[124] was used to evaluate the distribution of methylation across
1061 the genome. Next, a comparative analysis of the DMRs/DMCs across tissue types, contrasting
1062 the control and PMS samples was performed. In addition to the number of methylated tiles
1063 per annotation category was calculated, as well as their distance to the closest Transcription
1064 Start Site (TSS). To calculate the epigenetic age, we applied the Shireby-Cortex,[56] Hovarth,[57]
1065 and Zhang,[58] ageing clocks frameworks. For the Hovarth and Zhang estimations Clockbase
1066 platform[125] was used, relying on matched Illumina methyl array IDs. The DNA methylation

levels (0-100%) per CpG probe, and the sample metadata were submitted to Clockbase, and the predicted clock age was downloaded as CSV format. For the Shireby-Cortex[56] aging estimate, we downloaded the DNA methylation probes, and coefficient values and relied on matched Illumina methyl array IDs. We used total 347 DNA methylation CpG probes to predict epigenetic aging (> 20nts coverage).

Nuclei isolation, library preparation, and RNA sequencing

For the single-nucleus single-omics, (ATAC) and multiomics experiments, respectively, 2 x10^6 cells were harvested; nuclei were isolated following the manufacturer's instructions with minor modifications. Briefly, cells were lysed in 100 µL of freshly prepared lysis buffer (1 mM Tris-HCl [pH 7.4], 1 mM NaCl, 300 µM $MgCl_2$, 0.01% Tween-20, 0.01% IGEPAL CA-630, 0.001% Digitonin, 0.1% BSA, 100 µM DTT, and 100 mU/µL RNase inhibitor) for 1 minute on ice, washed twice in 500 µL of wash buffer (1 mM Tris-HCl [pH 7.4], 1 mM NaCl, 300 µM $MgCl_2$, 0.01% Tween-20, 0.1% BSA, 100 µM DTT, and 100 mU/µL RNase inhibitor), and the number of nuclei was assessed using the Countess II FL Automated Cell Counter (ThermoFisher). Thereafter, approximately 16,000 nuclei were incubated with the transposase enzyme, loaded into Chromium Next GEM Chip H Single Cell Kit (10x Genomics). snATAC libraries were generated using Chromium Single Cell ATAC Reagent Kits User Guide v1.1 (10x Genomics) according to manufacturer’s instructions; for the multi-omics samples, nuclei were loaded into Chromium Next GEM Chip J Single Cell Kit (10x Genomics); libraries were prepared using Chromium Next GEM Single Cell Multiome ATAC + Gene Expression Reagent Kits (10x Genomics) according to manufacturer’s instructions. The quality of the libraries was checked on the Agilent Bioanalyzer with High Sensitivity DNA kit (Agilent); per sample libraries were sequenced on Illumina Novaseq 6000 with target sequencing depths of 25,000 - 70,000 reads per nucleus.

For single-cell (sc)RNAseq, cells were counted using a hemocytometer, 10,000 cells were loaded into Chromium Next GEM Chip G Single Cell Kit (10x Genomics), and scRNA libraries were generated with Chromium Single Cell 3' Reagent Kits v3.1 (10x Genomics) according to manufacturer’s instructions. The quality of the libraries was checked on the 4200 Agilent Tapestation with High Sensitivity DNA kit (Agilent); per sample libraries were sequenced on Illumina Novaseq 6000 with target sequencing depths of 30,000 - 65,000 reads per cell.

Single-cell transcriptomics/ epigenetics data preprocessing

Standard CellRanger pipeline (6.1.2) and CellRanger ARC (2.0.0) were applied for aligning reads to the aforementioned version of the *H sapiens* genome and for quantifying gene/ peak expression. For the RNA component, intron-matching reads contributed to the gene

1103 expression levels. The processed gene expression matrix was imported in Seurat.[126]
1104 Additional filtering was performed on the distributions summarizing the number of counts,
1105 features, and percentages of reads incident to mitochondrial and ribosomal genes, across
1106 cells, per sample (accepted cells satisfied the criteria: number of UMIs > 8,000, number of
1107 genes per cell > 1,000, $\log_{10}$ (genes per UMI) > 0.75). We observed different ranges for MT
1108 and RP proportions for the scRNAseq and snRNAseq samples, respectively (we retained cells
1109 with 15-40% RP [scRNAseq] and 2-25% RP [snRNAseq]). Post-filtering, on all retained cells,
1110 the MT and RP entries were excluded from the expression matrix, pre-normalization. The
1111 normalization of expression levels was based on $\log_2$ normalization (scale.factor = 10000).
1112 The cell cycle assignation was performed in Seurat using the 'CellCycleScoring' function and
1113 *a priori* defined gene set.
1114
1115 *Clustering*
1116 Next, we applied the ClustAssess framework to determine optimal, data-driven parameters,
1117 starting with the number and type features according the stability of resulting partitions.[70] We
1118 used Element-centric similarity,[70] summarized on 30 iterations into Element centric
1119 consistency (ECC),[71] to objectively assess stability.[126] Highly variable features (N=1,000
1120 determined using the vst) approach, yielded optimal outputs. A 20-shared nearest neighbor
1121 (SNN) graph was constructed on the HGV PCA.[126] To address batch effect across sc and sn
1122 quantifications, we applied Harmony.[127] Clustering was performed using Louvain approach
1123 (resolution=0.2), implemented within Seurat[126] v4.0.5. 8 clusters produced a stable partition
1124 on scRNAseq and snRNAseq components. We excluded the smallest cluster (133 driven by
1125 a specific sample (i.e. C1-specific cluster). A X^2 test was used to assess the significance of
1126 proportions of cells for PMS *vs* control samples. Marker genes (on cluster *vs* complement and
1127 pairwise differential expression) were identified using the 'findMarker' function. The top 5 most
1128 positively differentially expressed genes were visualized in a heatmap.
1129 Enrichment analyses were performed using gprofiler[128] on markers called on a Wilcox test
1130 with a $|\log_2(FC)|$ threshold of 0.25, an adjusted p-value (Benjamini Hochberg multiple testing
1131 correction) less than 0.05 and a minimum percentage of cells expressing the gene of 0.1, in
1132 either subset. The background set for the enrichment analysis comprised all genes expressed
1133 in at least 10 cells.
1134
1135 *Voting Schemes*
1136 A variable voting-scheme was used to identify cell subsets requiring a minimum number of
1137 expressed genes corroborated with a minimum average expression level. The voting scheme
1138 for radial glial gene signature includes cells expressing 6 out of 9 manually curated genes
1139 (**Table S4**) with a normalized expression threshold of 1; glial progenitor cells express 7 out of

10 genes (**Table S4**) with an expression threshold of 0.5; neural progenitor cells express 5 out of 7 genes (**Table S4**) with an expression threshold of 0.5. The voting scheme for IFNα/β signaling is based on cells expressing 3 out of 6 genes (**Table S4**) with an expression threshold of 0.5; NOTCH1 signaling comprises cells expressing 13 out of 16 genes (**Table S4**) with no abundance threshold (I.e. presence/ absence).

Re-analysis of Absinta et al and Schirmer et al Data ex vivo datasets

Raw fastq files from the studies by *Schirmer et al.* (2019)[77] and *Absinta et al.* (2021)[16] were downloaded from ENA using fasterq-dump. The quality checking and mapping leading to the filtered feature-barcode matrices were performed as described above. For the *Schirmer et al.* (2019) dataset, cells with less than 4,000 features/genes were retained; an upper bound of 15,000 was employed for the maximum number of UMIs per cell; 5% is maximum proportion of fragments incident to mitochondrial DNA; 10% is the maximum proportion of reads incident to nuclear ribosomal genes. For *Absinta et al.* (2021), cells with the number of features between 200 and 5000 were kept for subsequent steps of the analysis; an upper threshold of 20,000 UMI counts was used, and the maximum mt% was set to 5%. Both datasets were normalized using SCTransform;[129] the *Absinta et al.* (2021) dataset was batch corrected using Harmony[127] on the patient variable, with θ = 2. To detect stable partitions, on each separate dataset, ClustAssess[70] was used with 20-50 iterations, assessing resolution parameters between 0.1 and 1.5 (0.1 increment steps). For the *Schirmer et al.* (2019) dataset, the top 4500 highly variable features yielded the most stable partitions; for the *Absinta et al.* (2021) dataset the top 3,500 highly variable features were selected. For both, the optimal resolution value was 0.6.

Pseudotime Analysis

Monocle3[130] was used to infer trajectories for the *in vitro* data, as well as for the single-cell data from the *Schirmer et al* and *Absinta et al* studies. To identify the start and the endpoint, a selection of genes was used in a voting approach. The manually curated set of genes, used for determining the starting region in the *in vitro* data, comprises TOP2A, CENPF, UBE2C, ASPM, APOLD1 with an expression threshold of 2 and a tolerance of 1 gene, i.e. any one gene from the set maybe not expressed; for the ending region, genes IFIT2 and CDKN2A were used, with an expression threshold of 1.5 and a tolerance of 0.

For the *Absinta et al* and *Schirmer et al*, larger subsets of genes were used; for the former, the following genes were used for the starting region: *LY6E*, *PPAN*, *FASN*, *CLU, SORD*, *TRAP1*, *TUBB2A*, *AP1S2*, *YBX3*, with an expression threshold of 0.5 and a tolerance of 4 genes; for the ending region, the following genes were used *ISG15*, *B4GALT5*, *IFITM3*, *SAR1A*, *KIAA1217*, *TRPC4*, *FGF4*, *B2M*, *ZC3HAV1*, *WARS*, *FN1*, *IFIT1*, with an expression

1177 threshold of 0.5 and a tolerance of 4 genes missing. For the *Schirmer et al* dataset, the ending
1178 region was defined by genes *ISG15*, *B4GALT5*, *IFITM3*, *SAR1A*, *KIAA1217*, *TRPC4*, *FGF4*,
1179 *B2M*, *ZC3HAV1*, *WARS*, *DDX58*, with an expression threshold of 0.5 and a tolerance of 6
1180 genes.
1181 Using the ordering of cells based on their transcriptomic signatures, the ClustAssess stability
1182 framework was applied on gene expression levels. This yielded a stable number of gene-
1183 clusters, named gene modules, representing a precursor of GRN inference; the genes per
1184 module were further characterized from a pathway perspective (using gprofiler[128]), against GO
1185 terms, KEGG and REAC terms, and functional elements (TFs and miRNAs). Next, we chose
1186 three gene modules that characterized sections of interest on the trajectory-based UMAPs of
1187 the *in vitro* dataset. The genes within each module were used to create a proxy (a
1188 transcriptomic pattern) subsequently employed to identify homologue gene modules
1189 computed based on the *ex vivo* datasets, *Schirmer et al* and *Absinta et al,* respectively. Briefly,
1190 we considered the percentage of genes present in the *ex vivo* gene modules using the three
1191 *in vitro* gene modules; to account for the variable number of genes for bo*th in vitro* and *ex vivo*
1192 modules the outputs are scaled by the size of the gene set, i.e. larger gene sets are penalized
1193 more than smaller gene sets. The pairwise comparison of gene modules (**Fig. S4A-D**) relies
1194 on Fisher's exact tests, using the *in vitro* data as baseline comparator. Benjamini-Hochber
1195 (FDR) correction was applied to account for the multiple testing pyscenic[131] was used to infer
1196 regulatory interactions, aligned with the metadata available for the *Homo sapiens* (hg38)
1197 reference genome. A docker container was used to generate a loom object from the existing
1198 Seurat object. Loompy was used[132] to create a SCope object, explored using the SCope web
1199 application; figure 6G illustrates specific regulons.
1200
1201 *Cell-cell regulatory interactions and effects*
1202 NicheNet[80] (v 2.0.4) was used to predict intercellular regulatory interactions, based on ligand-
1203 receptor databases (weighted_networks_nsga2r_final.rds). The correlative analysis,
1204 summarized as interaction scores, was applied on cluster-specific marker genes (differentially
1205 expressed genes). Further analyses were focused on cluster 5 ("inflammatory cluster")
1206 assigned as sender cells *vs* receiver cells, as the remaining clusters, respectively. The
1207 analysis was performed separately on control and PMS iNSCs, respectively. The summary of
1208 interactions was visualized using circos plot (circlize library v.0.4.15).
1209
1210 *Cytokine Array*
1211 iNSCs were plated at a density of 100,000 cells/cm^2 on GFR-coated plates. Media was
1212 collected on day 5 from each line. The Human Cytokine Antibody Array C5 (RayBiotech) was
1213 used for semi quantitative detection of 80 proteins according to manufacturer's instructions.

1214 Overnight incubation was performed for steps when the option was given. Membranes were
1215 exposed using a Gel Doc XR imager (BioRad). Blots were analyzed using the Protein Array
1216 Analyzer macro for ImageJ (written by Gilles Carpentier, 2008). The relative quantity of each
1217 protein was normalized to the positive and negative controls included on the array. The array
1218 was performed once for each iNSC line. Control lines were averaged together to generate a
1219 fold change comparison over PMS iNSC lines. To visualize the results, we calculate the Z-
1220 score per cytokine using the heatmap function in an R environment.
1221
1222 *snATACseq analysis*
1223 CellRanger ARC2.0.0 (multi-omics) and CellRanger ATAC2.0.0 (snATAC only) were used to
1224 map reads and quantify expression for the single nuclei ATAC-seq datasets. The peak calling
1225 was performed on pseudobulked input, comprising cells with at least 100 reads sequencing
1226 depth. Union peaks (peaks present in at least one sample) were reported. We excluded peaks
1227 overlapping the ENCODE-defined blacklist regions (hg38). To address the variation in
1228 sequencing depths, across samples, we normalized expression levels using random
1229 subsampling without replacement.[110] The set of fragments (with lengths varying from 200 to
1230 400 nts) *vs* the union-peaks were used to generate the ATAC expression matrix. For
1231 downstream analysis we relied onSeurat[126], Signac[133], and ArchR[134] packages. Additional
1232 quality controls include assessment of nucleosome signatures and TSS enrichment analysis.
1233 we filtered the fragments with nucleosome signals < 4 and TSS enrichment levels > 2. Peak
1234 intensities were normalized using the term frequency inverse document frequency (TF-IDF)
1235 normalization (scale factor = 10,000). The dimensionality reduction was performed using latent
1236 semantic indexing (LSI). Additionally, we performed Harmony integration across batches,
1237 which was used as input for the final clustering (resolution=0.2, SLM method[126]). Differentially
1238 expressed peaks were identified using the 'findMarker' function (Seurat package). We
1239 performed *de novo* motif analysis using Homer (*findMotifsGenome.pl*) and GO term
1240 enrichment analysis using GREAT with the background of the whole genome.[135]
1241
1242 *Integrative analysis of multimaps profiles*
1243 The integration of snRNAseq and snATACseq signals was performed on 5,242 cells with
1244 matched barcodes. The crosstalk between modalities was assessed using the partitioning
1245 information obtained on single modalities. The co-variation in expressed was summarized in
1246 joint ATAC/RNA heatmaps, with Z scores, calculated per modality, on pseudobulked
1247 expression per gene being presented for the gene itself (RNA modality), TSS proximal peaks
1248 (<3kb) and TSS distal peaks (greater than 3kb and less than 50kb). Both ATAC and RNA
1249 modalities were used to infer regulons using SCENIC+.[136]
1250

Statistical analysis

For all phenotypic analyses, a p-value < 0.05 was considered significant (*). We performed statistical tests described in individual figure legends using Prism software version 10 (GraphPad Software, San Diego CA). A Benjamini-Hochberg, False discovery rate (FDR) multiple testing correction was applied to account for Type I errors. For low throughput differential expression analysis on genes, we used a negative binomial test with the FDR cutoff value set to <0.05.

All analyses were performed on R 4.2.3, on high memory computer (MacPro M1 Max, 64GB memory) and servers (Intel E7-8860v4, 3TB memory).

REFERENCES

1. Reich, D.S., Lucchinetti, C.F., and Calabresi, P.A. (2018). Multiple Sclerosis. N Engl J Med *378*, 169-180. 10.1056/NEJMra1401483.

2. Giovannoni, G., Popescu, V., Wuerfel, J., Hellwig, K., Iacobaeus, E., Jensen, M.B., Garcia-Dominguez, J.M., Sousa, L., De Rossi, N., Hupperts, R., et al. (2022). Smouldering multiple sclerosis: the 'real MS'. Ther Adv Neurol Disord *15*, 17562864211066751. 10.1177/17562864211066751.

3. Graves, J.S., Krysko, K.M., Hua, L.H., Absinta, M., Franklin, R.J.M., and Segal, B.M. (2023). Ageing and multiple sclerosis. Lancet Neurol *22*, 66-77. 10.1016/S1474-4422(22)00184-3.

4. Hou, Y., Dan, X., Babbar, M., Wei, Y., Hasselbalch, S.G., Croteau, D.L., and Bohr, V.A. (2019). Ageing as a risk factor for neurodegenerative disease. Nat Rev Neurol *15*, 565-581. 10.1038/s41582-019-0244-7.

5. Papadopoulos, D., Magliozzi, R., Mitsikostas, D.D., Gorgoulis, V.G., and Nicholas, R.S. (2020). Aging, Cellular Senescence, and Progressive Multiple Sclerosis. Front Cell Neurosci *14*, 178. 10.3389/fncel.2020.00178.

6. Tian, Y.E., Cropley, V., Maier, A.B., Lautenschlager, N.T., Breakspear, M., and Zalesky, A. (2023). Heterogeneous aging across multiple organ systems and prediction of chronic disease and mortality. Nat Med *29*, 1221-1231. 10.1038/s41591-023-02296-6.

7. Cole, J.H., Raffel, J., Friede, T., Eshaghi, A., Brownlee, W.J., Chard, D., De Stefano, N., Enzinger, C., Pirpamer, L., Filippi, M., et al. (2020). Longitudinal Assessment of Multiple Sclerosis with the Brain-Age Paradigm. Ann Neurol *88*, 93-105. 10.1002/ana.25746.

8. Liao, Q., He, J., Tian, F.F., Bi, F.F., and Huang, K. (2022). A causal relationship between leukocyte telomere length and multiple sclerosis: A Mendelian randomization study. Front Immunol *13*, 922922. 10.3389/fimmu.2022.922922.

9. Krysko, K.M., Henry, R.G., Cree, B.A.C., Lin, J., University of California, S.F.M.S.E.T., Caillier, S., Santaniello, A., Zhao, C., Gomez, R., Bevan, C., et al. (2019). Telomere Length Is Associated with Disability Progression in Multiple Sclerosis. Ann Neurol *86*, 671-682. 10.1002/ana.25592.

10. Buhring, J., Hecker, M., Fitzner, B., and Zettl, U.K. (2021). Systematic Review of Studies on Telomere Length in Patients with Multiple Sclerosis. Aging Dis *12*, 1272-1286. 10.14336/AD.2021.0106.

11. Haider, L., Fischer, M.T., Frischer, J.M., Bauer, J., Hoftberger, R., Botond, G., Esterbauer, H., Binder, C.J., Witztum, J.L., and Lassmann, H. (2011). Oxidative damage in multiple sclerosis lesions. Brain *134*, 1914-1924. 10.1093/brain/awr128.

12. Dutta, R., McDonough, J., Yin, X., Peterson, J., Chang, A., Torres, T., Gudz, T., Macklin, W.B., Lewis, D.A., Fox, R.J., et al. (2006). Mitochondrial dysfunction as a cause of axonal degeneration in multiple sclerosis patients. Ann Neurol *59*, 478-489. 10.1002/ana.20736.

13. Campbell, G.R., Ziabreva, I., Reeve, A.K., Krishnan, K.J., Reynolds, R., Howell, O., Lassmann, H., Turnbull, D.M., and Mahad, D.J. (2011). Mitochondrial DNA deletions and neurodegeneration in multiple sclerosis. Ann Neurol *69*, 481-492. 10.1002/ana.22109.

14. Kular, L., Klose, D., Urdanoz-Casado, A., Ewing, E., Planell, N., Gomez-Cabrero, D., Needhamsen, M., and Jagodic, M. (2022). Epigenetic clock indicates accelerated aging in glial cells of progressive multiple sclerosis patients. Front Aging Neurosci *14*, 926468. 10.3389/fnagi.2022.926468.

15. Choi, I.Y., Lee, P., Adany, P., Hughes, A.J., Belliston, S., Denney, D.R., and Lynch, S.G. (2018). In vivo evidence of oxidative stress in brains of patients with progressive multiple sclerosis. Mult Scler *24*, 1029-1038. 10.1177/1352458517711568.

16. Absinta, M., Maric, D., Gharagozloo, M., Garton, T., Smith, M.D., Jin, J., Fitzgerald, K.C., Song, A., Liu, P., Lin, J.P., et al. (2021). A lymphocyte-microglia-astrocyte axis in chronic active multiple sclerosis. Nature. 10.1038/s41586-021-03892-7.

17. Nicaise, A.M., Wagstaff, L.J., Willis, C.M., Paisie, C., Chandok, H., Robson, P., Fossati, V., Williams, A., and Crocker, S.J. (2019). Cellular senescence in progenitor cells contributes to diminished remyelination potential in progressive multiple sclerosis. Proc Natl Acad Sci U S A *116*, 9030-9039. 10.1073/pnas.1818348116.

18. Jokubaitis, V.G., Campagna, M.P., Ibrahim, O., Stankovich, J., Kleinova, P., Matesanz, F., Hui, D., Eichau, S., Slee, M., Lechner-Scott, J., et al. (2022). Not all roads lead to the immune system: the genetic basis of multiple sclerosis severity. Brain. 10.1093/brain/awac449.

19. Lopez-Otin, C., Blasco, M.A., Partridge, L., Serrano, M., and Kroemer, G. (2023). Hallmarks of aging: An expanding universe. Cell *186*, 243-278. 10.1016/j.cell.2022.11.001.

20. Studer, L., Vera, E., and Cornacchia, D. (2015). Programming and Reprogramming Cellular Age in the Era of Induced Pluripotency. Cell Stem Cell *16*, 591-600. 10.1016/j.stem.2015.05.004.

21. Kabacik, S., Lowe, D., Fransen, L., Leonard, M., Ang, S.-L., Whiteman, C., Corsi, S., Cohen, H., Felton, S., Bali, R., et al. (2022). The relationship between epigenetic age and the hallmarks of aging in human cells. Nature Aging *2*, 484-493. 10.1038/s43587-022-00220-0.

22. Chomyk, A.M., Volsko, C., Tripathi, A., Deckard, S.A., Trapp, B.D., Fox, R.J., and Dutta, R. (2017). DNA methylation in demyelinated multiple sclerosis hippocampus. Sci Rep *7*, 8696. 10.1038/s41598-017-08623-5.

23. Huynh, J.L., Garg, P., Thin, T.H., Yoo, S., Dutta, R., Trapp, B.D., Haroutunian, V., Zhu, J., Donovan, M.J., Sharp, A.J., and Casaccia, P. (2014). Epigenome-wide differences in pathology-free regions of multiple sclerosis-affected brains. Nat Neurosci *17*, 121-130. 10.1038/nn.3588.

24. Mutukula, N., Man, Z., Takahashi, Y., Iniesta Martinez, F., Morales, M., Carreon-Guarnizo, E., Hernandez Clares, R., Garcia-Bernal, D., Martinez Martinez, L., Lajara, J., et al. (2021). Generation of RRMS and PPMS specific iPSCs as a platform for modeling Multiple Sclerosis. Stem Cell Res *53*, 102319. 10.1016/j.scr.2021.102319.

25. Ghirotto, B., Oliveira, D.F., Cipelli, M., Basso, P.J., de Lima, J., Breda, C.N.S., Ribeiro, H.C., Silva, C.C.C., Sertie, A.L., Oliveira, A.E.R., et al. (2022). MS-Driven Metabolic Alterations Are Recapitulated in iPSC-Derived Astrocytes. Ann Neurol *91*, 652-669. 10.1002/ana.26336.

26. Clayton, B.L.L., Barbar, L., Sapar, M., Rusielewicz, T., Kalpana, K., Migliori, B., Team, N.G.S.C.A., Paull, D., Brenner, K., Moroziewicz, D., et al. (2023). Patient iPSC models reveal glia-intrinsic phenotypes in multiple sclerosis. bioRxiv. 10.1101/2023.08.01.551553.

27. Obernier, K., and Alvarez-Buylla, A. (2019). Neural stem cells: origin, heterogeneity and regulation in the adult mammalian brain. Development *146*. 10.1242/dev.156059.

28. Gould, E., Reeves, A.J., Graziano, M.S., and Gross, C.G. (1999). Neurogenesis in the neocortex of adult primates. Science *286*, 548-552. 10.1126/science.286.5439.548.
29. Ponti, G., Peretto, P., and Bonfanti, L. (2008). Genesis of neuronal and glial progenitors in the cerebellar cortex of peripuberal and adult rabbits. PLoS One *3*, e2366. 10.1371/journal.pone.0002366.
30. Jhaveri, D.J., Tedoldi, A., Hunt, S., Sullivan, R., Watts, N.R., Power, J.M., Bartlett, P.F., and Sah, P. (2018). Evidence for newly generated interneurons in the basolateral amygdala of adult mice. Mol Psychiatry *23*, 521-532. 10.1038/mp.2017.134.
31. Ernst, A., Alkass, K., Bernard, S., Salehpour, M., Perl, S., Tisdale, J., Possnert, G., Druid, H., and Frisen, J. (2014). Neurogenesis in the striatum of the adult human brain. Cell *156*, 1072-1083. 10.1016/j.cell.2014.01.044.
32. Navarro Negredo, P., Yeo, R.W., and Brunet, A. (2020). Aging and Rejuvenation of Neural Stem Cells and Their Niches. Cell Stem Cell *27*, 202-223. 10.1016/j.stem.2020.07.002.
33. Encinas, J.M., Michurina, T.V., Peunova, N., Park, J.H., Tordo, J., Peterson, D.A., Fishell, G., Koulakov, A., and Enikolopov, G. (2011). Division-coupled astrocytic differentiation and age-related depletion of neural stem cells in the adult hippocampus. Cell Stem Cell *8*, 566-579. 10.1016/j.stem.2011.03.010.
34. Culig, L., Chu, X., and Bohr, V.A. (2022). Neurogenesis in aging and age-related neurodegenerative diseases. Ageing Res Rev *78*, 101636. 10.1016/j.arr.2022.101636.
35. Knoth, R., Singec, I., Ditter, M., Pantazis, G., Capetian, P., Meyer, R.P., Horvat, V., Volk, B., and Kempermann, G. (2010). Murine features of neurogenesis in the human hippocampus across the lifespan from 0 to 100 years. PLoS One *5*, e8809. 10.1371/journal.pone.0008809.
36. Wang, C., Liu, F., Liu, Y.Y., Zhao, C.H., You, Y., Wang, L., Zhang, J., Wei, B., Ma, T., Zhang, Q., et al. (2011). Identification and characterization of neuroblasts in the subventricular zone and rostral migratory stream of the adult human brain. Cell Res *21*, 1534-1550. 10.1038/cr.2011.83.
37. Gonzalez-Perez, O. (2012). Neural stem cells in the adult human brain. Biol Biomed Rep *2*, 59-69.
38. Sorrells, S.F., Paredes, M.F., Cebrian-Silla, A., Sandoval, K., Qi, D., Kelley, K.W., James, D., Mayer, S., Chang, J., Auguste, K.I., et al. (2018). Human hippocampal neurogenesis drops sharply in children to undetectable levels in adults. Nature *555*, 377-381. 10.1038/nature25975.
39. Tobin, M.K., Musaraca, K., Disouky, A., Shetti, A., Bheri, A., Honer, W.G., Kim, N., Dawe, R.J., Bennett, D.A., Arfanakis, K., and Lazarov, O. (2019). Human Hippocampal Neurogenesis Persists in Aged Adults and Alzheimer's Disease Patients. Cell Stem Cell *24*, 974-982 e973. 10.1016/j.stem.2019.05.003.
40. Hagihara, H., Murano, T., Ohira, K., Miwa, M., Nakamura, K., and Miyakawa, T. (2019). Expression of progenitor cell/immature neuron markers does not present definitive evidence for adult neurogenesis. Mol Brain *12*, 108. 10.1186/s13041-019-0522-8.
41. Sirko, S., Schichor, C., Della Vecchia, P., Metzger, F., Sonsalla, G., Simon, T., Burkle, M., Kalpazidou, S., Ninkovic, J., Masserdotti, G., et al. (2023). Injury-specific factors in the cerebrospinal fluid regulate astrocyte plasticity in the human brain. Nat Med *29*, 3149-3161. 10.1038/s41591-023-02644-6.

42. Snethen, H., Love, S., and Scolding, N. (2008). Disease-responsive neural precursor cells are present in multiple sclerosis lesions. Regen Med *3*, 835-847. 10.2217/17460751.3.6.835.
43. Nait-Oumesmar, B., Picard-Riera, N., Kerninon, C., Decker, L., Seilhean, D., Hoglinger, G.U., Hirsch, E.C., Reynolds, R., and Baron-Van Evercooren, A. (2007). Activation of the subventricular zone in multiple sclerosis: evidence for early glial progenitors. Proc Natl Acad Sci U S A *104*, 4694-4699. 10.1073/pnas.0606835104.
44. Wang, H., Yang, Y., Liu, J., and Qian, L. (2021). Direct cell reprogramming: approaches, mechanisms and progress. Nat Rev Mol Cell Biol *22*, 410-424. 10.1038/s41580-021-00335-z.
45. Meyer, S., Worsdorfer, P., Gunther, K., Thier, M., and Edenhofer, F. (2015). Derivation of Adult Human Fibroblasts and their Direct Conversion into Expandable Neural Progenitor Cells. J Vis Exp, e52831. 10.3791/52831.
46. Ionescu, R.-B., Nicaise, A.M., Reisz, J.A., Williams, E.C., Prasad, P., Dzieciatkowska, M., Stephenson, D., Cubero, M.S., Pirvan, L., Willis, C.M., et al. (2024). Increased Cholesterol Synthesis Drives Neurotoxicity in Patient Stem Cell-Derived Model of Multiple Sclerosis. bioRxiv, 2024.2001.2016.575826. 10.1101/2024.01.16.575826.
47. Moutsopoulos, I., Williams, E.C., and Mohorianu, II (2023). bulkAnalyseR: an accessible, interactive pipeline for analysing and sharing bulk multi-modal sequencing data. Brief Bioinform *24*. 10.1093/bib/bbac591.
48. Moutsopoulos, I., Maischak, L., Lauzikaite, E., Vasquez Urbina, S.A., Williams, E.C., Drost, H.G., and Mohorianu, II (2021). noisyR: enhancing biological signal in sequencing datasets by characterizing random technical noise. Nucleic Acids Res *49*, e83. 10.1093/nar/gkab433.
49. Love, M.I., Huber, W., and Anders, S. (2014). Moderated estimation of fold change and dispersion for RNA-seq data with DESeq2. Genome Biol *15*, 550. 10.1186/s13059-014-0550-8.
50. Robinson, M.D., McCarthy, D.J., and Smyth, G.K. (2010). edgeR: a Bioconductor package for differential expression analysis of digital gene expression data. Bioinformatics *26*, 139-140. 10.1093/bioinformatics/btp616.
51. Raudvere, U., Kolberg, L., Kuzmin, I., Arak, T., Adler, P., Peterson, H., and Vilo, J. (2019). g:Profiler: a web server for functional enrichment analysis and conversions of gene lists (2019 update). Nucleic Acids Res *47*, W191-W198. 10.1093/nar/gkz369.
52. Frisch, S.M., and MacFawn, I.P. (2020). Type I interferons and related pathways in cell senescence. Aging Cell *19*, e13234. 10.1111/acel.13234.
53. Park, H., Kim, C.H., Jeong, J.H., Park, M., and Kim, K.S. (2016). GDF15 contributes to radiation-induced senescence through the ROS-mediated p16 pathway in human endothelial cells. Oncotarget *7*, 9634-9644. 10.18632/oncotarget.7457.
54. Moiseeva, V., Cisneros, A., Sica, V., Deryagin, O., Lai, Y., Jung, S., Andres, E., An, J., Segales, J., Ortet, L., et al. (2023). Senescence atlas reveals an aged-like inflamed niche that blunts muscle regeneration. Nature *613*, 169-178. 10.1038/s41586-022-05535-x.
55. Huang, W., Hickson, L.J., Eirin, A., Kirkland, J.L., and Lerman, L.O. (2022). Cellular senescence: the good, the bad and the unknown. Nat Rev Nephrol *18*, 611-627. 10.1038/s41581-022-00601-z.
56. Shireby, G.L., Davies, J.P., Francis, P.T., Burrage, J., Walker, E.M., Neilson, G.W.A., Dahir, A., Thomas, A.J., Love, S., Smith, R.G., et al. (2020). Recalibrating the epigenetic clock: implications for assessing biological age in the human cortex. Brain *143*, 3763-3775. 10.1093/brain/awaa334.

57. Horvath, S. (2013). DNA methylation age of human tissues and cell types. Genome Biol *14*, R115. 10.1186/gb-2013-14-10-r115.
58. Zhang, Q., Vallerga, C.L., Walker, R.M., Lin, T., Henders, A.K., Montgomery, G.W., He, J., Fan, D., Fowdar, J., Kennedy, M., et al. (2019). Improved precision of epigenetic clock estimates across tissues and its implication for biological ageing. Genome Med *11*, 54. 10.1186/s13073-019-0667-1.
59. Dolatabadi, S., Jonasson, E., Andersson, L., Luna Santamaria, M., Linden, M., Osterlund, T., Aman, P., and Stahlberg, A. (2022). FUS-DDIT3 Fusion Oncoprotein Expression Affects JAK-STAT Signaling in Myxoid Liposarcoma. Front Oncol *12*, 816894. 10.3389/fonc.2022.816894.
60. Kidani, Y., Elsaesser, H., Hock, M.B., Vergnes, L., Williams, K.J., Argus, J.P., Marbois, B.N., Komisopoulou, E., Wilson, E.B., Osborne, T.F., et al. (2013). Sterol regulatory element-binding proteins are essential for the metabolic programming of effector T cells and adaptive immunity. Nat Immunol *14*, 489-499. 10.1038/ni.2570.
61. Hennighausen, L., and Robinson, G.W. (2008). Interpretation of cytokine signaling through the transcription factors STAT5A and STAT5B. Genes Dev *22*, 711-721. 10.1101/gad.1643908.
62. Bailey, C.M., Abbott, D.E., Margaryan, N.V., Khalkhali-Ellis, Z., and Hendrix, M.J. (2008). Interferon regulatory factor 6 promotes cell cycle arrest and is regulated by the proteasome in a cell cycle-dependent manner. Mol Cell Biol *28*, 2235-2243. 10.1128/MCB.01866-07.
63. Nyati, K.K., and Kishimoto, T. (2021). Recent Advances in the Role of Arid5a in Immune Diseases and Cancer. Front Immunol *12*, 827611. 10.3389/fimmu.2021.827611.
64. International Multiple Sclerosis Genetics, C. (2019). Multiple sclerosis genomic map implicates peripheral immune cells and microglia in susceptibility. Science *365*. 10.1126/science.aav7188.
65. International Multiple Sclerosis Genetics, C. (2013). Network-based multiple sclerosis pathway analysis with GWAS data from 15,000 cases and 30,000 controls. Am J Hum Genet *92*, 854-865. 10.1016/j.ajhg.2013.04.019.
66. Hussman, J.P., Beecham, A.H., Schmidt, M., Martin, E.R., McCauley, J.L., Vance, J.M., Haines, J.L., and Pericak-Vance, M.A. (2016). GWAS analysis implicates NF-kappaB-mediated induction of inflammatory T cells in multiple sclerosis. Genes Immun *17*, 305-312. 10.1038/gene.2016.23.
67. Kristjansdottir, G., Sandling, J.K., Bonetti, A., Roos, I.M., Milani, L., Wang, C., Gustafsdottir, S.M., Sigurdsson, S., Lundmark, A., Tienari, P.J., et al. (2008). Interferon regulatory factor 5 (IRF5) gene variants are associated with multiple sclerosis in three distinct populations. J Med Genet *45*, 362-369. 10.1136/jmg.2007.055012.
68. Hatami, M., Salmani, T., Arsang-Jang, S., Davood Omrani, M., Mazdeh, M., Ghafouri-Fard, S., Sayad, A., and Taheri, M. (2018). STAT5a and STAT6 gene expression levels in multiple sclerosis patients. Cytokine *106*, 108-113. 10.1016/j.cyto.2017.10.022.
69. Shang, Z., Sun, W., Zhang, M., Xu, L., Jia, X., Zhang, R., and Fu, S. (2020). Identification of key genes associated with multiple sclerosis based on gene expression data from peripheral blood mononuclear cells. PeerJ *8*, e8357. 10.7717/peerj.8357.
70. Shahsavari, A., Munteanu, A., and Mohorianu, I. (2022). ClustAssess: tools for assessing the robustness of single-cell clustering. bioRxiv, 2022.2001.2031.478592. 10.1101/2022.01.31.478592.

71. Gates, A.J., Wood, I.B., Hetrick, W.P., and Ahn, Y.Y. (2019). Element-centric clustering comparison unifies overlaps and hierarchy. Sci Rep *9*, 8574. 10.1038/s41598-019-44892-y.

72. Eze, U.C., Bhaduri, A., Haeussler, M., Nowakowski, T.J., and Kriegstein, A.R. (2021). Single-cell atlas of early human brain development highlights heterogeneity of human neuroepithelial cells and early radial glia. Nat Neurosci *24*, 584-594. 10.1038/s41593-020-00794-1.

73. Chamling, X., Kallman, A., Fang, W., Berlinicke, C.A., Mertz, J.L., Devkota, P., Pantoja, I.E.M., Smith, M.D., Ji, Z., Chang, C., et al. (2021). Single-cell transcriptomic reveals molecular diversity and developmental heterogeneity of human stem cell-derived oligodendrocyte lineage cells. Nat Commun *12*, 652. 10.1038/s41467-021-20892-3.

74. Marques, S., van Bruggen, D., Vanichkina, D.P., Floriddia, E.M., Munguba, H., Varemo, L., Giacomello, S., Falcao, A.M., Meijer, M., Bjorklund, A.K., et al. (2018). Transcriptional Convergence of Oligodendrocyte Lineage Progenitors during Development. Dev Cell *46*, 504-517 e507. 10.1016/j.devcel.2018.07.005.

75. Darmanis, S., Sloan, S.A., Zhang, Y., Enge, M., Caneda, C., Shuer, L.M., Hayden Gephart, M.G., Barres, B.A., and Quake, S.R. (2015). A survey of human brain transcriptome diversity at the single cell level. Proc Natl Acad Sci U S A *112*, 7285-7290. 10.1073/pnas.1507125112.

76. Luciani, M., Garsia, C., Beretta, S., Petiti, L., Peano, C., Merelli, I., Cifola, I., Miccio, A., Meneghini, V., and Gritti, A. (2023). Human iPSC-derived neural stem cells display a radial glia-like signature in vitro and favorable long-term safety in transplanted mice. bioRxiv, 2023.2008.2004.551937. 10.1101/2023.08.04.551937.

77. Schirmer, L., Velmeshev, D., Holmqvist, S., Kaufmann, M., Werneburg, S., Jung, D., Vistnes, S., Stockley, J.H., Young, A., Steindel, M., et al. (2019). Neuronal vulnerability and multilineage diversity in multiple sclerosis. Nature *573*, 75-82. 10.1038/s41586-019-1404-z.

78. Saul, D., Kosinsky, R.L., Atkinson, E.J., Doolittle, M.L., Zhang, X., LeBrasseur, N.K., Pignolo, R.J., Robbins, P.D., Niedernhofer, L.J., Ikeno, Y., et al. (2022). A new gene set identifies senescent cells and predicts senescence-associated pathways across tissues. Nat Commun *13*, 4827. 10.1038/s41467-022-32552-1.

79. Johnson, C.A., and Ghashghaei, H.T. (2020). Sp2 regulates late neurogenic but not early expansive divisions of neural stem cells underlying population growth in the mouse cortex. Development *147*. 10.1242/dev.186056.

80. Browaeys, R., Saelens, W., and Saeys, Y. (2020). NicheNet: modeling intercellular communication by linking ligands to target genes. Nat Methods *17*, 159-162. 10.1038/s41592-019-0667-5.

81. Imayoshi, I., Sakamoto, M., Yamaguchi, M., Mori, K., and Kageyama, R. (2010). Essential roles of Notch signaling in maintenance of neural stem cells in developing and adult brains. J Neurosci *30*, 3489-3498. 10.1523/JNEUROSCI.4987-09.2010.

82. Borghi, A., Verstrepen, L., and Beyaert, R. (2016). TRAF2 multitasking in TNF receptor-induced signaling to NF-kappaB, MAP kinases and cell death. Biochem Pharmacol *116*, 1-10. 10.1016/j.bcp.2016.03.009.

83. Belenguer, G., Duart-Abadia, P., Jordan-Pla, A., Domingo-Muelas, A., Blasco-Chamarro, L., Ferron, S.R., Morante-Redolat, J.M., and Farinas, I. (2021). Adult Neural Stem Cells Are Alerted by Systemic Inflammation through TNF-alpha Receptor Signaling. Cell Stem Cell *28*, 285-299 e289. 10.1016/j.stem.2020.10.016.

84. Coppe, J.P., Desprez, P.Y., Krtolica, A., and Campisi, J. (2010). The senescence-associated secretory phenotype: the dark side of tumor suppression. Annu Rev Pathol *5*, 99-118. 10.1146/annurev-pathol-121808-102144.
85. Munoz-Fontela, C., Macip, S., Martinez-Sobrido, L., Brown, L., Ashour, J., Garcia-Sastre, A., Lee, S.W., and Aaronson, S.A. (2008). Transcriptional role of p53 in interferon-mediated antiviral immunity. J Exp Med *205*, 1929-1938. 10.1084/jem.20080383.
86. Schauder, D.M., Shen, J., Chen, Y., Kasmani, M.Y., Kudek, M.R., Burns, R., and Cui, W. (2021). E2A-regulated epigenetic landscape promotes memory CD8 T cell differentiation. Proc Natl Acad Sci U S A *118*. 10.1073/pnas.2013452118.
87. Kandhaya-Pillai, R., Miro-Mur, F., Alijotas-Reig, J., Tchkonia, T., Kirkland, J.L., and Schwartz, S. (2017). TNFalpha-senescence initiates a STAT-dependent positive feedback loop, leading to a sustained interferon signature, DNA damage, and cytokine secretion. Aging (Albany NY) *9*, 2411-2435. 10.18632/aging.101328.
88. Van de Sande, B., Flerin, C., Davie, K., De Waegeneer, M., Hulselmans, G., Aibar, S., Seurinck, R., Saelens, W., Cannoodt, R., Rouchon, Q., et al. (2020). A scalable SCENIC workflow for single-cell gene regulatory network analysis. Nat Protoc *15*, 2247-2276. 10.1038/s41596-020-0336-2.
89. Factor, D.C., Barbeau, A.M., Allan, K.C., Hu, L.R., Madhavan, M., Hoang, A.T., Hazel, K.E.A., Hall, P.A., Nisraiyya, S., Najm, F.J., et al. (2020). Cell Type-Specific Intralocus Interactions Reveal Oligodendrocyte Mechanisms in MS. Cell *181*, 382-395 e321. 10.1016/j.cell.2020.03.002.
90. International Multiple Sclerosis Genetics, C., and Multiple, M.S.C. (2023). Locus for severity implicates CNS resilience in progression of multiple sclerosis. Nature *619*, 323-331. 10.1038/s41586-023-06250-x.
91. Unnikrishnan, A., Hadad, N., Masser, D.R., Jackson, J., Freeman, W.M., and Richardson, A. (2018). Revisiting the genomic hypomethylation hypothesis of aging. Ann N Y Acad Sci *1418*, 69-79. 10.1111/nyas.13533.
92. Campagna, M.P., Xavier, A., Lea, R.A., Stankovich, J., Maltby, V.E., Butzkueven, H., Lechner-Scott, J., Scott, R.J., and Jokubaitis, V.G. (2022). Whole-blood methylation signatures are associated with and accurately classify multiple sclerosis disease severity. Clin Epigenetics *14*, 194. 10.1186/s13148-022-01397-2.
93. Roy, E., and Cao, W. (2022). Glial interference: impact of type I interferon in neurodegenerative diseases. Mol Neurodegener *17*, 78. 10.1186/s13024-022-00583-3.
94. Rasa, S.M.M., Annunziata, F., Krepelova, A., Nunna, S., Omrani, O., Gebert, N., Adam, L., Kappel, S., Hohn, S., Donati, G., et al. (2022). Inflammaging is driven by upregulation of innate immune receptors and systemic interferon signaling and is ameliorated by dietary restriction. Cell Rep *39*, 111017. 10.1016/j.celrep.2022.111017.
95. Gulen, M.F., Samson, N., Keller, A., Schwabenland, M., Liu, C., Gluck, S., Thacker, V.V., Favre, L., Mangeat, B., Kroese, L.J., et al. (2023). cGAS-STING drives ageing-related inflammation and neurodegeneration. Nature *620*, 374-380. 10.1038/s41586-023-06373-1.
96. Tabula Muris, C. (2020). A single-cell transcriptomic atlas characterizes ageing tissues in the mouse. Nature *583*, 590-595. 10.1038/s41586-020-2496-1.
97. Xie, X., Ma, G., Li, X., Zhao, J., Zhao, Z., and Zeng, J. (2023). Activation of innate immune cGAS-STING pathway contributes to Alzheimer's pathogenesis in 5xFAD mice. Nat Aging *3*, 202-212. 10.1038/s43587-022-00337-2.

98. Standaert, D.G., and Childers, G.M. (2022). Alpha-synuclein-mediated DNA damage, STING activation, and neuroinflammation in Parkinson's disease. Proc Natl Acad Sci U S A *119*, e2204058119. 10.1073/pnas.2204058119.
99. Levine, K.S., Leonard, H.L., Blauwendraat, C., Iwaki, H., Johnson, N., Bandres-Ciga, S., Ferrucci, L., Faghri, F., Singleton, A.B., and Nalls, M.A. (2023). Virus exposure and neurodegenerative disease risk across national biobanks. Neuron *111*, 1086-1093 e1082. 10.1016/j.neuron.2022.12.029.
100. Bjornevik, K., Cortese, M., Healy, B.C., Kuhle, J., Mina, M.J., Leng, Y., Elledge, S.J., Niebuhr, D.W., Scher, A.I., Munger, K.L., and Ascherio, A. (2022). Longitudinal analysis reveals high prevalence of Epstein-Barr virus associated with multiple sclerosis. Science *375*, 296-301. 10.1126/science.abj8222.
101. Wilkins, J.M., Gakh, O., Kabiraj, P., McCarthy, C.B., Tobin, W.O., Howe, C.L., and Lucchinetti, C.F. (2020). Signatures of cell stress and altered bioenergetics in skin fibroblasts from patients with multiple sclerosis. Aging (Albany NY) *12*, 15134-15156. 10.18632/aging.103612.
102. Kury, P., Nath, A., Creange, A., Dolei, A., Marche, P., Gold, J., Giovannoni, G., Hartung, H.P., and Perron, H. (2018). Human Endogenous Retroviruses in Neurological Diseases. Trends Mol Med *24*, 379-394. 10.1016/j.molmed.2018.02.007.
103. Garza, R., Sharma, Y., Atacho, D.A.M., Thiruvalluvan, A., Abu Hamdeh, S., Jonsson, M.E., Horvath, V., Adami, A., Ingelsson, M., Jern, P., et al. (2023). Single-cell transcriptomics of human traumatic brain injury reveals activation of endogenous retroviruses in oligodendroglia. Cell Rep *42*, 113395. 10.1016/j.celrep.2023.113395.
104. Lin, B., Coleman, J.H., Peterson, J.N., Zunitch, M.J., Jang, W., Herrick, D.B., and Schwob, J.E. (2017). Injury Induces Endogenous Reprogramming and Dedifferentiation of Neuronal Progenitors to Multipotency. Cell Stem Cell *21*, 761-774 e765. 10.1016/j.stem.2017.09.008.
105. Absinta, M., Sati, P., Masuzzo, F., Nair, G., Sethi, V., Kolb, H., Ohayon, J., Wu, T., Cortese, I.C.M., and Reich, D.S. (2019). Association of Chronic Active Multiple Sclerosis Lesions With Disability In Vivo. JAMA Neurol *76*, 1474-1483. 10.1001/jamaneurol.2019.2399.
106. Preziosa, P., Pagani, E., Meani, A., Moiola, L., Rodegher, M., Filippi, M., and Rocca, M.A. (2022). Slowly Expanding Lesions Predict 9-Year Multiple Sclerosis Disease Progression. Neurol Neuroimmunol Neuroinflamm *9*. 10.1212/NXI.0000000000001139.
107. Douvaras, P., and Fossati, V. (2015). Generation and isolation of oligodendrocyte progenitor cells from human pluripotent stem cells. Nat Protoc *10*, 1143-1154. 10.1038/nprot.2015.075.
108. Ewels, P., Magnusson, M., Lundin, S., and Kaller, M. (2016). MultiQC: summarize analysis results for multiple tools and samples in a single report. Bioinformatics *32*, 3047-3048. 10.1093/bioinformatics/btw354.
109. Shen, W., Le, S., Li, Y., and Hu, F. (2016). SeqKit: A Cross-Platform and Ultrafast Toolkit for FASTA/Q File Manipulation. PLoS One *11*, e0163962. 10.1371/journal.pone.0163962.
110. Mohorianu, I., Bretman, A., Smith, D.T., Fowler, E.K., Dalmay, T., and Chapman, T. (2017). Comparison of alternative approaches for analysing multi-level RNA-seq data. PLoS One *12*, e0182694. 10.1371/journal.pone.0182694.
111. Dobin, A., Davis, C.A., Schlesinger, F., Drenkow, J., Zaleski, C., Jha, S., Batut, P., Chaisson, M., and Gingeras, T.R. (2013). STAR: ultrafast universal RNA-seq aligner. Bioinformatics *29*, 15-21. 10.1093/bioinformatics/bts635.

112. Liao, Y., Smyth, G.K., and Shi, W. (2014). featureCounts: an efficient general purpose program for assigning sequence reads to genomic features. Bioinformatics *30*, 923-930. 10.1093/bioinformatics/btt656.
113. Danecek, P., Bonfield, J.K., Liddle, J., Marshall, J., Ohan, V., Pollard, M.O., Whitwham, A., Keane, T., McCarthy, S.A., Davies, R.M., and Li, H. (2021). Twelve years of SAMtools and BCFtools. Gigascience *10*. 10.1093/gigascience/giab008.
114. Bolstad, B.M., Irizarry, R.A., Astrand, M., and Speed, T.P. (2003). A comparison of normalization methods for high density oligonucleotide array data based on variance and bias. Bioinformatics *19*, 185-193. 10.1093/bioinformatics/19.2.185.
115. Huynh-Thu, V.A., Irrthum, A., Wehenkel, L., and Geurts, P. (2010). Inferring regulatory networks from expression data using tree-based methods. PLoS One *5*. 10.1371/journal.pone.0012776.
116. Almende, B., Thieurmel, B., and Robert, T. (2019). Package 'visnetwork'.
117. Joglekar, M.V., Satoor, S.N., Wong, W.K.M., Cheng, F., Ma, R.C.W., and Hardikar, A.A. (2020). An Optimised Step-by-Step Protocol for Measuring Relative Telomere Length. Methods Protoc *3*. 10.3390/mps3020027.
118. Kechin, A., Boyarskikh, U., Kel, A., and Filipenko, M. (2017). cutPrimers: A New Tool for Accurate Cutting of Primers from Reads of Targeted Next Generation Sequencing. J Comput Biol *24*, 1138-1143. 10.1089/cmb.2017.0096.
119. Kim, D., Paggi, J.M., Park, C., Bennett, C., and Salzberg, S.L. (2019). Graph-based genome alignment and genotyping with HISAT2 and HISAT-genotype. Nat Biotechnol *37*, 907-915. 10.1038/s41587-019-0201-4.
120. Krueger, F., and Andrews, S.R. (2011). Bismark: a flexible aligner and methylation caller for Bisulfite-Seq applications. Bioinformatics *27*, 1571-1572. 10.1093/bioinformatics/btr167.
121. Akalin, A., Kormaksson, M., Li, S., Garrett-Bakelman, F.E., Figueroa, M.E., Melnick, A., and Mason, C.E. (2012). methylKit: a comprehensive R package for the analysis of genome-wide DNA methylation profiles. Genome Biol *13*, R87. 10.1186/gb-2012-13-10-r87.
122. Juhling, F., Kretzmer, H., Bernhart, S.H., Otto, C., Stadler, P.F., and Hoffmann, S. (2016). metilene: fast and sensitive calling of differentially methylated regions from bisulfite sequencing data. Genome Res *26*, 256-262. 10.1101/gr.196394.115.
123. McCullagh, P., and Nelder, J.A. (1998). Generalized linear models, 2nd Edition (Chapman & Hall/CRC).
124. Heinz, S., Benner, C., Spann, N., Bertolino, E., Lin, Y.C., Laslo, P., Cheng, J.X., Murre, C., Singh, H., and Glass, C.K. (2010). Simple combinations of lineage-determining transcription factors prime cis-regulatory elements required for macrophage and B cell identities. Mol Cell *38*, 576-589. 10.1016/j.molcel.2010.05.004.
125. Ying, K., Tyshkovskiy, A., Trapp, A., Liu, H., Moqri, M., Kerepesi, C., and Gladyshev, V.N. (2023). ClockBase: ClockBase: a comprehensive platform for biological age profiling in human and mouse. bioRxiv. https://doi.org/10.1101/2023.02.28.530532.
126. Hao, Y., Hao, S., Andersen-Nissen, E., Mauck, W.M., 3rd, Zheng, S., Butler, A., Lee, M.J., Wilk, A.J., Darby, C., Zager, M., et al. (2021). Integrated analysis of multimodal single-cell data. Cell *184*, 3573-3587 e3529. 10.1016/j.cell.2021.04.048.
127. Korsunsky, I., Millard, N., Fan, J., Slowikowski, K., Zhang, F., Wei, K., Baglaenko, Y., Brenner, M., Loh, P.R., and Raychaudhuri, S. (2019). Fast, sensitive and accurate integration of single-cell data with Harmony. Nat Methods *16*, 1289-1296. 10.1038/s41592-019-0619-0.

128. Kolberg, L., Raudvere, U., Kuzmin, I., Vilo, J., and Peterson, H. (2020). gprofiler2 -- an R package for gene list functional enrichment analysis and namespace conversion toolset g:Profiler. F1000Res *9*. 10.12688/f1000research.24956.2.
129. Hafemeister, C., and Satija, R. (2019). Normalization and variance stabilization of single-cell RNA-seq data using regularized negative binomial regression. Genome Biol *20*, 296. 10.1186/s13059-019-1874-1.
130. Qiu, X., Mao, Q., Tang, Y., Wang, L., Chawla, R., Pliner, H.A., and Trapnell, C. (2017). Reversed graph embedding resolves complex single-cell trajectories. Nat Methods *14*, 979-982. 10.1038/nmeth.4402.
131. Aibar, S., Gonzalez-Blas, C.B., Moerman, T., Huynh-Thu, V.A., Imrichova, H., Hulselmans, G., Rambow, F., Marine, J.C., Geurts, P., Aerts, J., et al. (2017). SCENIC: single-cell regulatory network inference and clustering. Nat Methods *14*, 1083-1086. 10.1038/nmeth.4463.
132. Wolf, F.A., Angerer, P., and Theis, F.J. (2018). SCANPY: large-scale single-cell gene expression data analysis. Genome Biol *19*, 15. 10.1186/s13059-017-1382-0.
133. Stuart, T., Srivastava, A., Madad, S., Lareau, C.A., and Satija, R. (2021). Single-cell chromatin state analysis with Signac. Nat Methods *18*, 1333-1341. 10.1038/s41592-021-01282-5.
134. Granja, J.M., Corces, M.R., Pierce, S.E., Bagdatli, S.T., Choudhry, H., Chang, H.Y., and Greenleaf, W.J. (2021). ArchR is a scalable software package for integrative single-cell chromatin accessibility analysis. Nat Genet *53*, 403-411. 10.1038/s41588-021-00790-6.
135. McLean, C.Y., Bristor, D., Hiller, M., Clarke, S.L., Schaar, B.T., Lowe, C.B., Wenger, A.M., and Bejerano, G. (2010). GREAT improves functional interpretation of cis-regulatory regions. Nat Biotechnol *28*, 495-501. 10.1038/nbt.1630.
136. Bravo Gonzalez-Blas, C., De Winter, S., Hulselmans, G., Hecker, N., Matetovici, I., Christiaens, V., Poovathingal, S., Wouters, J., Aibar, S., and Aerts, S. (2023). SCENIC+: single-cell multiomic inference of enhancers and gene regulatory networks. Nat Methods *20*, 1355-1367. 10.1038/s41592-023-01938-4.